THE ASTROPHYSICAL JOURNAL SUPPLEMENT SERIES, 126:85–103, 2000 January
© 2000. The American Astronomical Society. All rights reserved. Printed in U.S.A.

A MID-INFRARED GALAXY ATLAS (MIGA)

C. R. KERTON[1] AND P. G. MARTIN
Canadian Institute for Theoretical Astrophysics, University of Toronto, Toronto, Ontario M5S 3H8, Canada;
kerton@cita.utoronto.ca, pgmartin@cita.utoronto.ca
Received 1999 April 20; accepted 1999 August 16

ABSTRACT

A mid-infrared atlas of part of the Galactic plane ($75° < l < 148°$, $b = \pm 6°$) has been constructed using HIRES processed infrared data to provide a mid-infrared data set for the Canadian Galactic Plane Survey (CGPS). The addition of this data set to the CGPS will enable the study of the emission from the smallest components of interstellar dust at an angular resolution comparable to that of the radio, millimeter, and far-infrared data in the CGPS. The Mid-Infrared Galaxy Atlas (MIGA) is a mid-infrared (12 and 25 μm) counterpart to the far-infrared *IRAS* Galaxy Atlas (IGA), and consists of resolution enhanced ($\sim 0\farcm5$ resolution) HIRES images along with ancillary maps. This paper describes the processing and characteristics of the atlas, the cross-band simulation technique used to obtain high-resolution ratio maps, and future plans to extend both the IGA and MIGA.

Subject headings: atlases — dust, extinction — Galaxy: structure — infrared: galaxies — techniques: image processing

1. INTRODUCTION

The Mid-Infrared Galaxy Atlas (MIGA) is a mid-infrared (12 and 25 μm) atlas of part of the Galactic plane ($75° < l < 148°$, $b = \pm 6°$). It was constructed using *IRAS* data processed to approximately $0\farcm5$ resolution using the HIRES image construction process (Aumann, Fowler, & Melnyk 1990) including a new point source ringing suppression algorithm (Cao, Eggermont, & Terebey 1999). Parts of the MIGA along with the far-infrared (60 and 100 μm) *IRAS* Galaxy Atlas (IGA; Cao et al. 1997) are being merged with radio and millimeter data as part of the Canadian Galactic Plane Survey (English et al. 1998a; CGPS[2]), a project to survey about a quadrant of the Galactic plane at $\leq 1'$ resolution over a wide range of wavelengths (12 μm–190 cm) to study all of the major components of the interstellar medium (ISM).

The addition of a mid-infrared data set to this database is important since one of the goals of the CGPS is to understand the evolution of dust as it moves through different phases of the ISM. The 25 and 12 μm bands of *IRAS* have been shown to be good tracers of the smallest dust particles: the chemically uncharacterized very small grains (VSGs) and the large carbonaceous molecules, most likely polycyclic aromatic hydrocarbons (PAHs) (Onaka et al. 1996), respectively. Therefore, the MIGA will enable the study of the emission from the smallest components of interstellar dust at an angular resolution comparable to that of the complementary data being used to define different physical environments.

This paper has been designed to be complementary to the paper describing the IGA (Cao et al. 1997). Many of the details of the image construction algorithms for the MIGA and the IGA are identical and were described in great detail in a series of papers related to both the IGA and the parallelization of the HIRES code (Cao et al. 1997; Cao et al. 1996); thus, they will not be repeated here. Rather we concentrate on pointing out those areas where the MIGA and IGA differ (most importantly in resolution behavior and the response to point sources) and on demonstrating through a series of tests on the data that the MIGA is a data set of comparable quality to the IGA. This paper, combined with the papers describing the IGA, gives a complete guide to the infrared data sets that will be made available to the general astronomical community as part of the CGPS data releases over the next few years. The information provided in this paper is relevant to both MIGA mosaicked images included in the CGPS and stand-alone MIGA images.

In § 2 we describe the format of the atlas along with the format of an extension to the IGA (EIGA; for Extended IGA) that was constructed specifically for the CGPS. The steps involved in MIGA processing are outlined in § 3. Section 4 describes the characteristics of MIGA images. In § 5 various artifacts of the images are discussed, including the reduced point source ringing. Finally, sample images are shown in § 6, and future directions for the MIGA and large-scale HIRES processing are discussed in § 7.

2. DESCRIPTION OF THE ATLAS—MIGA AND EIGA

The atlas covers a 12° wide strip ($b = \pm 6°$) of the Galactic plane from Cygnus to Cassiopeia ($75° < l < 148°$). The higher latitude limit, compared to the IGA ($b = \pm 4\fdg7$), was required to match the MIGA with the CGPS coverage which extends from $-3\fdg56 < b < 5\fdg56$ in order to follow the main concentration of H I in this part of the Galaxy. With this upper bound set, the lower boundary of the atlas was chosen to be symmetric.

Each MIGA image covers a $1\fdg4 \times 1\fdg4$ area and consists of first and twentieth iteration HIRES images along with 10 ancillary maps and tables as listed in Table 1. See Figures 1 and 2 for sample images. The images are in Galactic Cartesian (CAR) projection[3] with a pixel size of 15″. MIGA images are quite flexible; users can make seamless mosaics of arbitrary size (see § 6) and rebin and reproject the images

[1] Also at Department of Astronomy, University of Toronto.

[2] Current information on the CGPS can be found at http://www.ras.ucalgary.ca/CGPS/.

[3] Greisen, E. W., & Calabretta, M. 1996, draft available from the NRAO FITS archive at http://www.cv.nrao.edu/fits/.

TABLE 1

MIGA Atlas Files

File Type[a]	Description
bem_*	Image showing location of point sources used to generate img_*bem* files
cfv_*	Correction factor variance, first and twentieth iteration
cvg_*	Coverage
det_*.....	Detector tracks
img_*	First and twentieth iteration HIRES images
img_*bem*.....	Beam maps, first and twentieth iteration
phn_*.....	Photometric noise, first and twentieth iteration
*fwhm.txt	Tabulation of two-dimensional Gaussian fits to twentieth iteration beams

[a] The asterisk (*) refers to text in the file name that gives the image wavelength (12 or 25 μm), iteration, and/or location (CRRD plate number and Galactic coordinates).

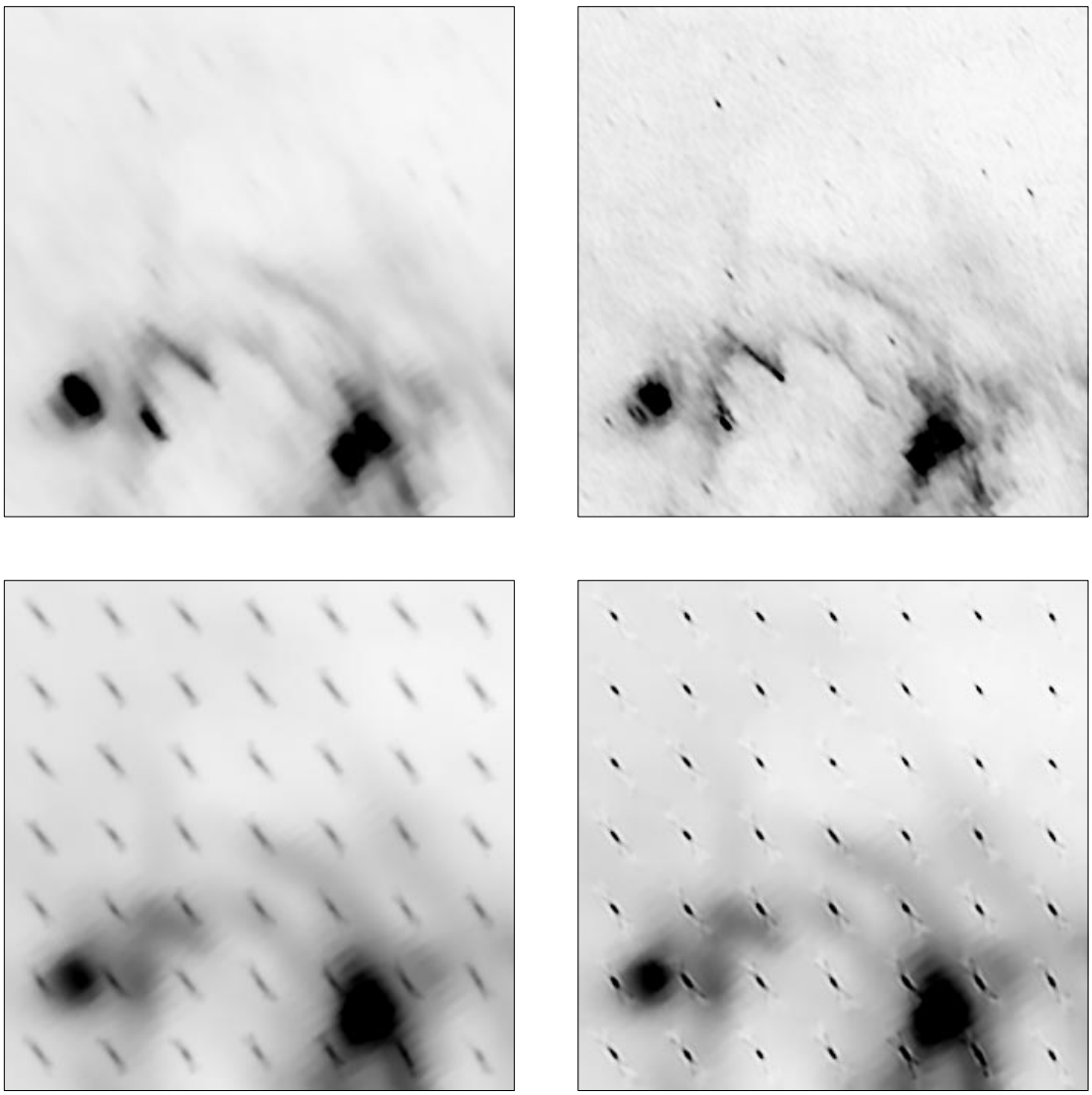

Fig. 1.—Image and beam maps at 12 μm associated with the $1\overset{\circ}{.}4 \times 1\overset{\circ}{.}4$ area centered at $l = 138°$, $b = 2\overset{\circ}{.}0$ (part of the H II region W5 East). The upper row shows the first (*left*) and twentieth iteration HIRES images for the area. The lower row shows the beam maps for the area. The background used for processing the beam maps is a smoothed version of the twentieth iteration HIRES image.

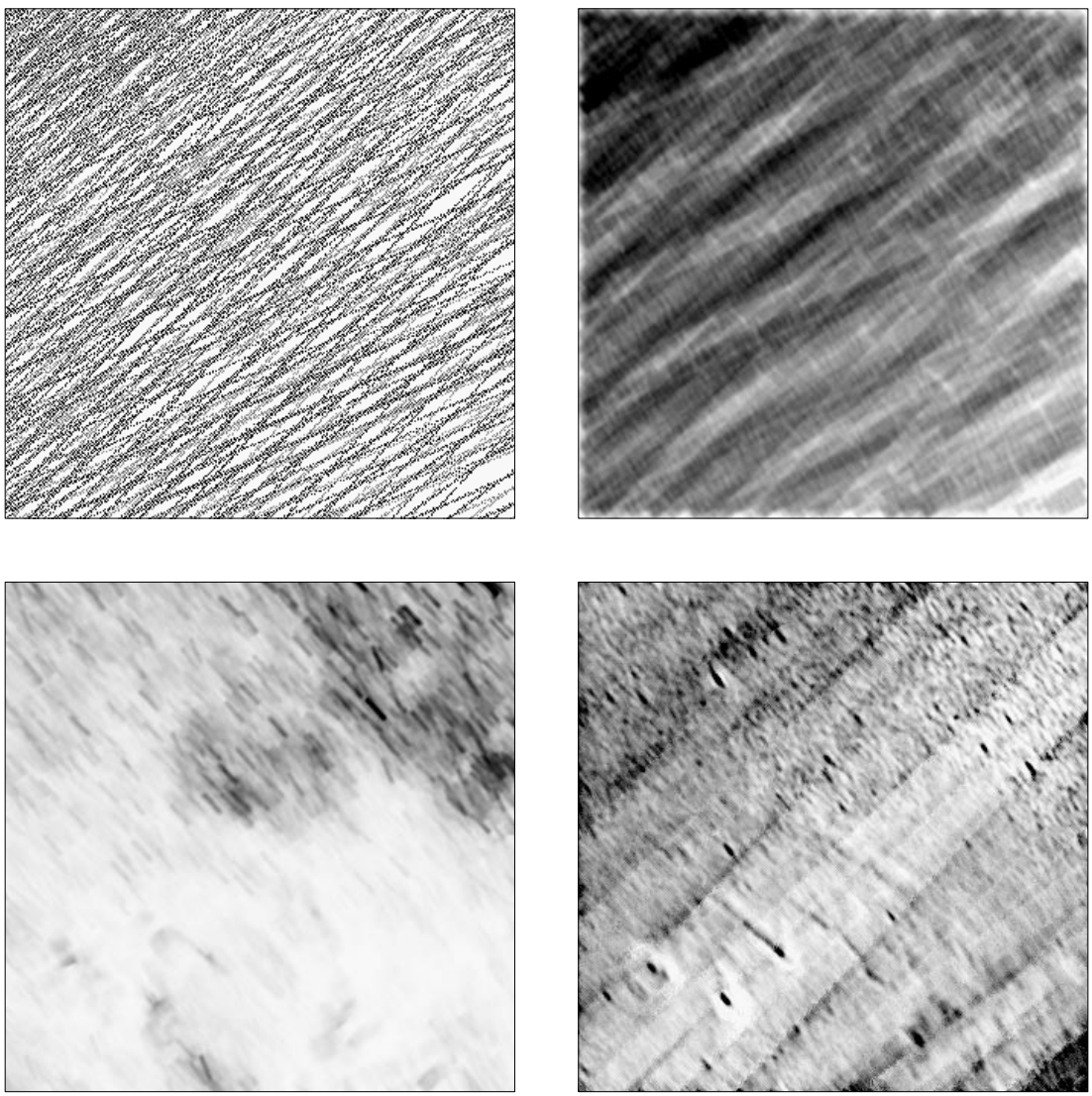

FIG. 2.—Ancillary files associated with the same area as in Fig. 1. Clockwise from the upper left: det_*, cvg_*, phn_* (20), and cfv_* (20). The detector track map (det_*) shows the scan pattern of the *IRAS* detectors. The coverage map (cvg_*) is created by combining the detector response patterns with the det_* map (dark areas show regions of high coverage). The narrow trim of low coverage (white) seen in this image is caused by data points that lie partially outside the processed area and were thus entirely rejected (images are trimmed before mosaicking to avoid any problems with such low coverage). The phn_* map provides a measure of the relative noise across an image (black for higher noise). Its value is calculated by propagating the a priori noise assigned to a given *IRAS* measurement to the image grid. The cfv_* map provides a measure of the relative fitting error, i.e., how much the image has changed from the previous iteration (black for a larger error/change). A large value indicates poor, noisy data or saturated regions. A high value may also indicate that the source is not as fully resolved as possible (Aumann et al. 1990; Cao et al. 1996).

as required. The full data set is available on tape from the Canadian Institute for Theoretical Astrophysics (CITA).[4]

Part of the MIGA, a series of $5\overset{\circ}{.}12 \times 5\overset{\circ}{.}12$ mosaics, will be available on the web through the Canadian Astronomy Data Centre (CADC)[5] as part of the general public release of the CGPS data. The CGPS mosaics have a pixel size of 18″, and so the MIGA and IGA images were slightly rebinned in creating these mosaics. The CGPS mosaics will be a very useful way to access both the MIGA and IGA data, particularly since users will have immediate access to complementary radio and millimeter data on a uniform grid covering the same region. Tests done on regular and rebinned MIGA images show that there is little reduction in the quality of the images due to the slight rebinning. The general image characteristics described here for the MIGA, and in Cao et al. (1997) for the IGA, apply equally to the MIGA and IGA in the CGPS mosaic format.

Since the IGA has a high-latitude cutoff of $b = 4\overset{\circ}{.}7$ the initial CGPS mosaics constructed using the IGA had a blank strip at high latitudes. In order to match the infrared coverage of the CGPS with the radio coverage we constructed a high-latitude extension to the IGA covering $75^\circ < l < 148^\circ$ and $4\overset{\circ}{.}7 < b < 5\overset{\circ}{.}56$. Agreement between the original IGA images and the EIGA is excellent and the EIGA has been incorporated into all of the CGPS far-infrared mosaics (see § 7). This ability to extend the infrared images of the IGA and the MIGA to higher/lower Galactic latitudes is an important reason why HIRES and the *IRAS*

[4] http://www.cita.utoronto.ca/.
[5] http://cadcwww.hia.nrc.ca/.

database, with its almost full-sky coverage, remains an important tool to study the infrared sky. This will be discussed more in § 7.

3. DESCRIPTION OF PROCESSING

The basic processing of the MIGA (and EIGA) follows the same steps as discussed in detail in Cao et al. (1997). The raw *IRAS* archive data, known as CRDD (Calibrated Reconstructed Detector Data) were first sent from IPAC to CITA to allow processing to be done locally. The raw data are uncompressed and formatted using the programs SnipScan and LAUNDR. The data are processed in $7^\circ \times 7^\circ$ sections known as CRDD plates.

Infrared Sky Survey Atlas (ISSA) images corresponding to the plate region are mosaicked together and used to calibrate the *IRAS* data using the SmLAUN program. This program first creates simulated *IRAS* data by scanning the ISSA plates with the known *IRAS* scan pattern for the region. Then the median difference between each CRDD value and the simulated data within 1° (along the scan line) is calculated and subtracted. This step effectively removes the zodiacal emission since ISSA images have a zodiacal light model subtracted from them. Uncertainties in this model, and the effect these uncertainties have on the quality of the MIGA, are discussed in § 4.5. ISSA mosaicking was done in advance of the other preprocessing steps to allow the quality of the mosaicking to be checked before use (see § 5). The data are then reprojected from equatorial coordinates to Galactic coordinates using the BrkDet program. At this stage the data are in $1\overset{\circ}{.}4 \times 1\overset{\circ}{.}4$ sections spaced every 1°. All of the preprocessing steps were done on a Sparc Ultra workstation. For a single CRDD plate preprocessing took on average about 2 hours of wall clock time to complete in addition to the time required to construct and check the ISSA mosaics. To cover the CGPS region 63 CRDD plates in two bands had to be processed ($\sim$240 hr).

These data are then HIRES processed to create the final images and ancillary maps. Unlike the IGA, we used a nonparallel version of the HIRES code on a SGI Origin 2000 computer at CITA. The original HIRES code was first modified to run on the SGI architecture and tests were made comparing IGA release images to 60 and 100 μm images constructed at CITA. IGA images were recreated for a field at $l = 152^\circ$, $b = -1^\circ$ using the new code and no differences were seen, beyond that expected for numerical round-off errors: maximum fractional differences were on the order of 10^{-5} and average fractional differences were on the order of 10^{-8}.

The construction of the EIGA gave us another chance to test the new code for compatibility with the IGA production code. As shown in § 7 the match between the IGA images and the EIGA images produced at CITA is excellent.

Tests showed that processing a single $1\overset{\circ}{.}4 \times 1\overset{\circ}{.}4$ region at a given wavelength took approximately 4.5 minutes of wall clock time. While this is clearly slower than the processing times reported in Cao et al. (1996) for the parallel-processing machines, it is a vast improvement over the single-processor times they report. Since we were primarily interested in covering the CGPS survey region which contains 444 $1\overset{\circ}{.}4 \times 1\overset{\circ}{.}4$ areas, and considering other overheads in the production, this processing speed was adequate. It took 67 hours of wall clock time to process the entire CGPS region at both 12 and 25 μm (about a quarter of the time required to prepare the CRDD data on the Sparc Ultra).

The HIRES code we used also took advantage of a ringing suppression algorithm that was developed after the IGA was in its production run (Cao et al. 1999). Tests were done before producing the MIGA to compare the quality of the images with and without the ringing suppression algorithm in place. Differences between the two images were negligible away from point sources. In § 5.1 we discuss the effect of the ringing suppression algorithm on point sources in more detail.

4. CHARACTERISTICS OF THE IMAGES

In this section of the paper we describe the resolution, photometric accuracy, positional accuracy, surface brightness accuracy, and the mosaic property of the MIGA.

4.1. *Resolution*

The basic angular size of the rectangular *IRAS* detectors is $45'' \times 270''$ at 12 μm and $45'' \times 276''$ at 25 μm (Aumann et al. 1990). The higher resolution is obtained along the scan direction of the satellite. As a result of different scan orientations the position angle of the elongated raw beam varies across the sky. Improved resolution is possible because each region is covered by overlapping scans and was usually revisited with a different scan orientation (see Fig. 2).

In order to assess the achieved resolution of the MIGA within each field simulated beams (PSFs) are constructed using the HIRES *IRAS* Simulator mode (Fowler & Aumann 1994). Spikes are placed in a regular grid on a smoothed version of the twentieth image. As discussed in Cao et al. (1997), the image histogram is used to scale the spikes to an intensity that represents a point source that is bright enough, relative to the background emission, that HIRES processing is beneficial. The image is then scanned with the detector pattern to produce simulated *IRAS* data. These data are then regularly HIRES processed to produce the img_*bem* maps that show the *IRAS* beam shape (see Fig. 1). As will be discussed below, while the results of a two-dimensional Gaussian fit to these beams does give a measure of the resolution (*fwhm.txt files), the actual beam shapes are not two-dimensional Gaussians even when the beams are not X-shaped due to large differences in the scan directions (Rice 1993; Moshir et al. 1992).

To quantify the MIGA resolution we sampled 12 fields scattered across the atlas region, using the FWHM of two-dimensional Gaussian fits to simulated beams as a measure of the achieved resolution. The results of this test are shown in Table 2 where we report the mean and standard deviation about the mean for the 49 beams in each field. The average resolution for the 12 test fields is $33'' \times 67''$ and $34'' \times 66''$ at 12 and 25 μm, respectively. This should be compared with the typical full-resolution co-add (FRESCO; equivalent to first iteration MIGA and IGA images) resolution of $1' \times 5'$ in both wavebands or the standardized ISSA resolution of $4' \times 5'$ in all wavebands. The pixel size of $15''$ just adequately samples the beam in the scan direction.

One important thing to notice is the similarity of the resolution at 12 and 25 μm. Within any given field the resolution may vary from place to place, but the 12 and 25 μm resolutions are always very close in value. The position angles of the beams are also very close; in a test of 756 simulated 12 and 25 μm beams the difference between the

TABLE 2

RESOLUTION TEST

	MAJOR AXIS—12 μm		MINOR AXIS—12 μm		MAJOR AXIS—25 μm		MINOR AXIS—25 μm	
FIELD[a]	FWHM[b] (arcsec)	St. Dev.	FWHM (arcsec)	St. Dev.	FWHM (arcsec)	St. Dev.	FWHM (arcsec)	St. Dev.
g075+02.....	74.24	5.48	33.65	2.70	72.81	6.25	34.24	2.44
g077−04.....	76.37	4.06	34.98	2.17	75.29	3.76	35.86	1.74
g084+03.....	51.55	10.4	41.33	5.51	50.02	10.3	39.31	4.82
g094−06.....	57.59	5.52	28.14	2.38	58.76	7.48	29.69	3.30
g107+05.....	55.45	6.79	33.33	2.84	57.12	7.27	34.82	3.15
g133+00.....	70.90	5.61	32.14	2.65	71.67	6.77	32.18	2.31
g115−01.....	67.63	6.13	32.41	2.10	66.80	6.37	33.02	2.01
g116−02.....	64.73	6.74	31.43	2.08	64.29	6.80	32.39	2.46
g118+02.....	66.57	4.78	32.27	1.99	64.65	6.04	32.67	2.94
g119−01.....	69.55	5.59	32.90	1.77	70.22	5.74	33.59	2.23
g123−06.....	64.96	6.40	29.98	2.20	60.47	8.15	29.90	2.02
g138+04.....	80.57	4.28	35.73	2.08	82.51	3.64	36.65	2.15
Average[c]	66.7±2.5		33.2±0.9		66.2±2.6		33.7±0.8	

[a] Field notation indicates the field center in Galactic coordinates.
[b] FWHM reported is the average of 49 beams in each field; their standard deviation is given in the adjacent column.
[c] Average ± standard deviation of the mean.

position angles was on average 0°.07. Figure 3 shows the FWHM fits to beams on one of the MIGA fields of Table 2 along with the same data for the corresponding IGA field. MIGA has a better resolution than the IGA. The resolution between the two MIGA bands is very well matched at all locations in the image. The situation is quite different for the 60 and 100 μm bands of the IGA where the resolution and the position angle of the beams varies considerably between the two bands. In a test of 756 simulated 100 and 60 μm beams the difference between the position angles was on average 7°. The reason for this behavior is that the mid-infrared detectors on the *IRAS* focal plane have the same physical size, whereas the sizes of the far-infrared detectors differ, and that the mid-infrared detectors are packed more closely together in the focal plane than the far-infrared detectors so that their scan pattern on the sky is more similar (see the *IRAS* Explanatory Supplement 1988 for details on the *IRAS* detectors and the layout of the focal plane).

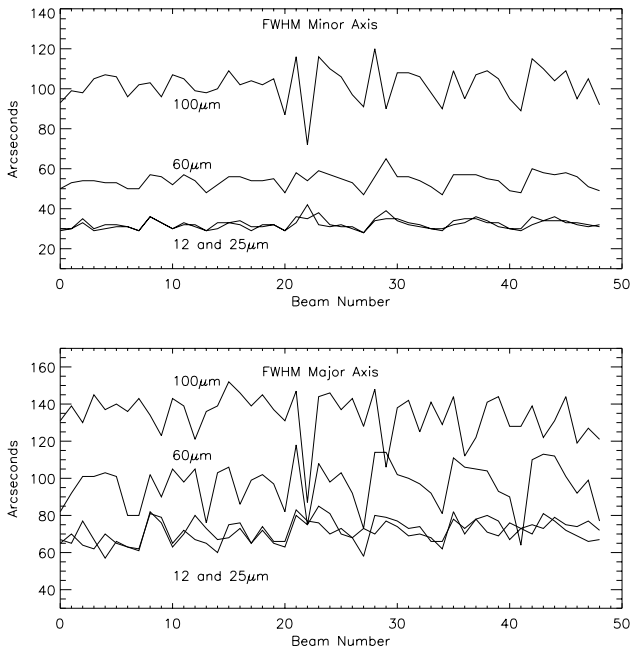

FIG. 3.—Comparison of the achieved resolution of MIGA and IGA images for the 1°.4 × 1°.4 region centered at $l = 115°$, $b = 0°$. Values plotted are the FWHM of two-dimensional Gaussian fits to the simulated HIRES beams at 49 locations (distributed evenly in a 7 × 7 grid) in the image. Notice the large difference in resolution between the two IGA bands (100 and 60 μm). In contrast, the resolution of the two MIGA bands (12 and 25 μm) is closely matched at all locations in the image. The point sources used to construct the simulated beams have been scaled and have been processed at different background levels. This factor causes most of the variation in FWHM between 12 and 25 μm for a given point source (see text and Fig. 5 for details).

The resolution achieved in HIRES processing is a function of the number of iterations, the coverage pattern, and the strength of the point source relative to the background value *during processing*. The latter two factors are what cause the scatter in resolution seen at a given wavelength in Figure 3. The best resolution, for a given coverage, is achieved for a high ratio of point source strength to background which is why a bias level is applied to the image during HIRES processing to bring the background level of the image as close to zero as possible (see § 3.5 of Cao et al. 1997 for more details regarding the calculation of the flux bias). The bias level that is applied to a given MIGA image is reported in the image header as a flux in units of W m^{-2}. This value can be converted to an intensity (in Jy sr^{-1}) by dividing the value by the average detector solid angle (3.2×10^{-7} sr at 12 μm and 3.5×10^{-7} sr at 25 μm; Moshir et al. 1992) and by a factor that accounts for the *IRAS* bandpass shape (1.348×10^{-13} and 5.16×10^{-14} (Hz) at 12 and 25 μm, respectively). These bandpass factors were derived using the assumption of a source spectrum with the shape $\nu I_\nu = \text{constant}$ (see the *IRAS* Explanatory Supplement 1988 for details).

In order to examine the variation of resolution with changing point source to local processing background ratio (PS/BG) for the MIGA we created simulated beam maps for the 1°.4 × 1°.4 field centered at $l = 74°$, $b = -6°$ using point sources with fluxes of 0.05 to 10,000 Jy. In this region the average background level was fairly low, 2.32 and 6.43 MJy

sr^{-1} at 12 and 25 μm, respectively. These values can be converted to a flux using the average detector solid angles yielding average background fluxes of 0.74 and 2.2 Jy, respectively. To simplify the test we did not apply a flux bias during processing, and so these were the background values for HIRES processing. The results of this test are shown in Figure 4. These two plots illustrate that the resolution of a point source is not dependent on just the strength of the source but the ratio PS/BG. In the upper plot one sees that for most of the point sources in this test the resolution achieved at 12 μm is slightly better than at 25 μm, but this is only because of the lower processing background used at 12 μm. In the lower panel we illustrate this directly by plotting the same resolution measurements for both 12 and 25 μm against PS/BG. All of the data follow the expected trend of increasing resolution with increasing point source strength to background ratio. The slight difference in the loci followed by the 12 and 25 μm points is probably due to the combination of two factors. The first is that differences in the sky structure between each wavelength can cause the measured resolution to vary slightly. The other is that there are small differences in the 12 and 25 μm beam shape even for identical scan patterns because the detectors were placed in slightly different locations on the *IRAS* focal plane.

In Figure 5 we replot the data from Figure 3 now showing the FWHM achieved as a function of PS/BG. Values for the point source intensity (PS) and local background intensity are reported in the *fwhm.txt files for each field. To obtain the local background during processing

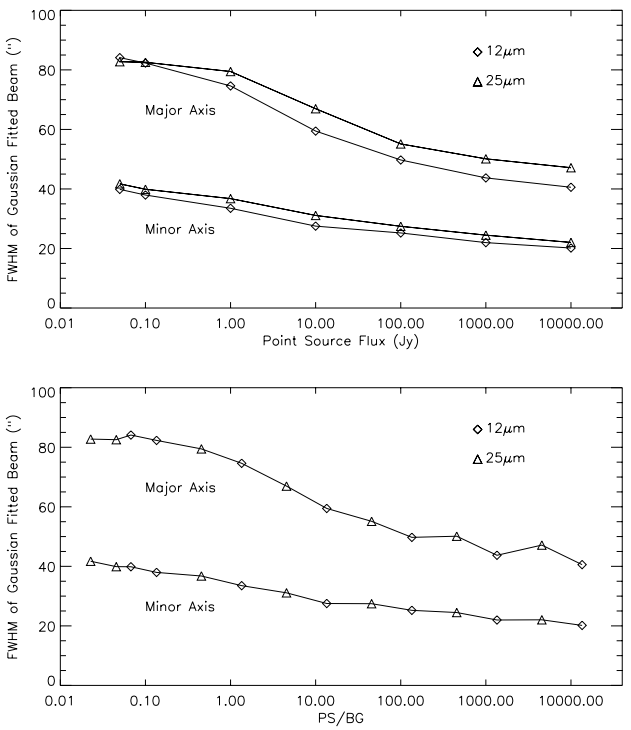

FIG. 4.—Dependence of beam resolution on source and background flux (BG). In the top figure we show the resolution as a function of the point source strength (PS). At any given PS, the ratio PS/BG is higher at 12 μm than at 25 μm due to the lower 12 μm background level, and this results in a better resolution at 12 μm. In the lower figure we show this directly by plotting the same data points as a function of the PS/BG. The resolution of the HIRES beam improves steadily in both bands as PS/BG increases. Each point shown is the average value for 49 simulated beams evenly arrayed in a test field located at $l = 74°$, $b = -6°$.

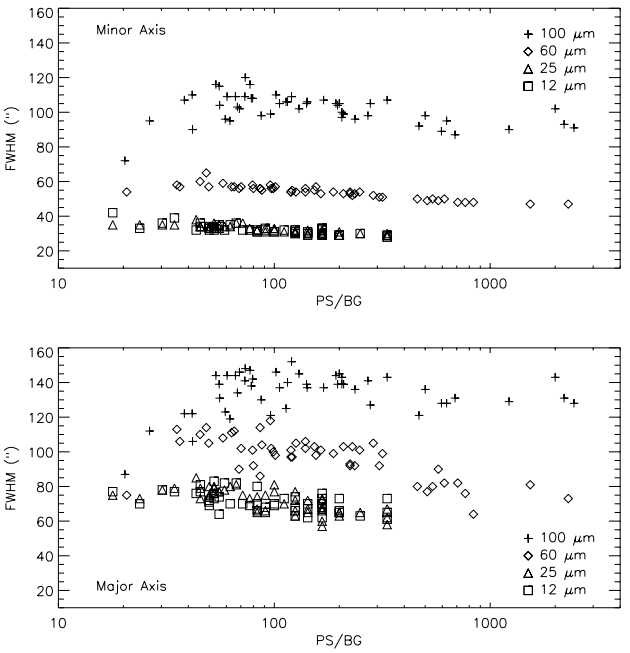

FIG. 5.—Data from Fig. 3 replotted as a function of the ratio of point source flux to background flux *during HIRES processing* (PS/BG). The match in resolution at 12 and 25 μm holds over a wide range of PS/BG.

(BG) we subtracted the flux bias value reported in the images header from the local background. The difference in resolution between the far and mid-infrared *IRAS* bands, and the match in resolution between the 12 and 25 μm bands, holds over a wide range in PS/BG. Figure 5 also shows that the trend of increasing resolution with increasing PS/BG is very flat, so that point sources with a range of PS/BG will still have similar achieved resolutions at 12 and 25 μm. Although the beam simulations are done with a realistic assessment of the processing background for the actual image, still the resolutions reported in the *fwhm.txt files are for a particular injected point source and so are only representative of the resolution in the actual images.

4.2. *Ratio Maps and Cross-band Simulation*

This similarity in resolution between the two bands means that, with care, high-resolution ratio maps can be created directly using the MIGA images. Care is required because, although the FWHM fits to the simulated beams are very close, the actual beam shapes are not two-dimensional Gaussians and can vary in detail because of the actual PS/BG in the two images. As an example, Figure 6 shows two ratio maps of the region around the H II region S151, chosen because of the unusual irregular cross-shaped beam pattern caused by the significant difference in the scan angle between the two *IRAS* coverages of the region (this effect is more noticeable at high ecliptic latitudes). The first image was constructed by simply dividing the 12 μm MIGA image by the 25 μm MIGA image.

The other ratio map was constructed using a technique called cross-band simulation (Fowler & Aumann 1994). This technique makes use of the HIRES *IRAS* simulator mode. First the simulator scans the 12 μm HIRES image with the 25 μm detector pattern to create a simulated view of the 12 μm sky. These "observations" are then regularly HIRES processed to create a somewhat lower resolution

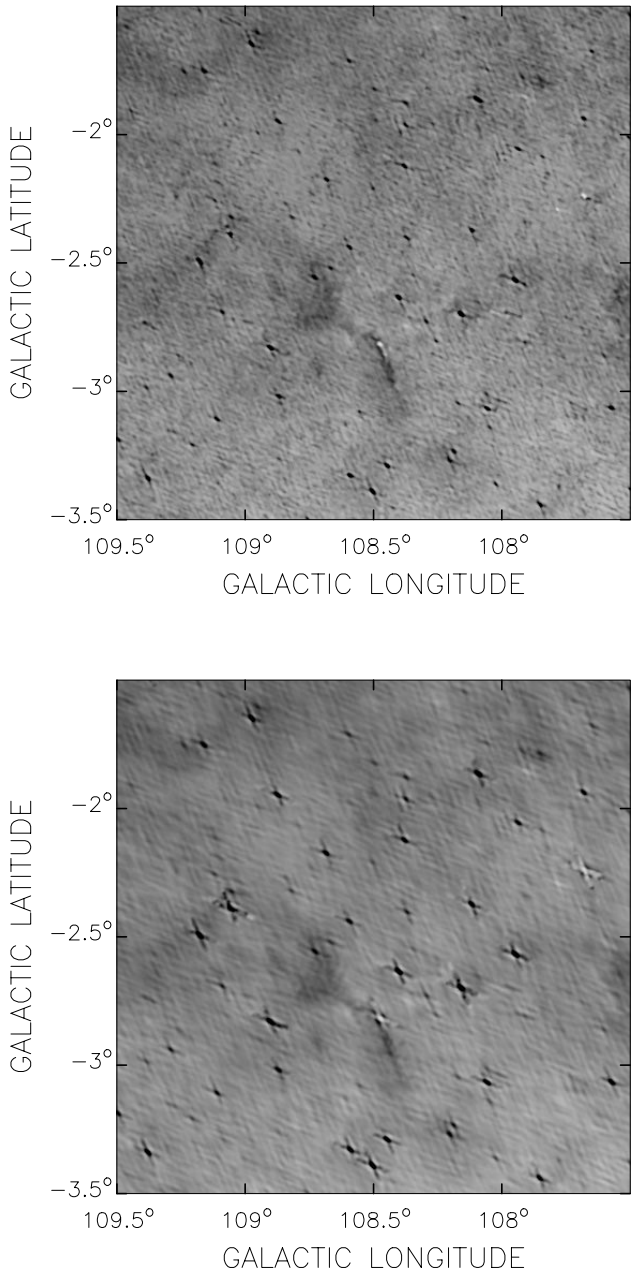

FIG. 6.—Comparison of ratio maps (12/25) constructed using a simple division of MIGA images (*top*) and using the HIRES *IRAS* Simulator to perform cross-band beam matching (*bottom*). Images are linearly stretched from 0 (*white*) to 1 (*black*). This causes most of the point sources (stars) to saturate and appear as black structures since they are brighter at 12 μm than at 25 μm. The two noticeable exceptions are the point source associated with S151 at $l = 108.5$, $b = -2.8$ and the point source at $l = 107.6$, $b = -2.24$ (the planetary nebula PK 107−2.1). In general structure shown in each image is the same, but that the point sources are more clearly defined in the bottom image because of the matching beam shapes. For example, the feature associated with S151 is more clearly shown to be a point source in the beam-matched image than in the simple ratio image. The lower image also has a less mottled background due to the matched beams and the slightly lower resolution.

version of the 12 μm image. The same process is followed for the 25 μm data. The final result is two images at the same resolution (slightly poorer than the original 25 μm) with almost identical beam shapes. The effect of bringing the two wavebands to the same beam shape is seen in the way the point sources (cross-shaped beam pattern) in Figure 6 are undistorted in the cross-band simulator image, while the point sources show some nonphysical structure in the original.

The cross-band simulation does not compensate for differing PS/BG that may occur between the two bands. For the most demanding work, say in examining a particular part of an image with vastly different PS/BG, flux biases could be chosen to better match PS/BG locally. However, for some purposes even the simple MIGA ratio map may suffice. The user should closely inspect the simulated beam maps to determine if the beam shapes are close enough for their purposes. If so, the common resolution of the MIGA provides a quick and easy way to obtain high-resolution mid-infrared ratio maps. Note that any simple ratio map involving the IGA will not be as satisfactory, and cross-band simulation will be desirable. Therefore, we are developing an algorithm to do this using (M)IGA and its ancillary data, rather than having to return to the raw *IRAS* data.

4.3. *Photometry*

In order to test the photometric accuracy achieved in the MIGA images we selected 52 point sources scattered across the range of the atlas. Sources selected were bright (>10 Jy in each band), isolated, and resolved (as indicated by the point source template correlation coefficient in the *IRAS* Point Source Catalog [PSC]). While the maximum-correlation method (MCM; Aumann et al. 1990) algorithm at the heart of HIRES conserves flux globally the flux can be redistributed across the image with each iteration causing changes in the measured flux at a given location.

Photometry was done using a script driving the IPAC Skyview program.[6] Circular apertures of radius 5′ and 7′ were drawn around each point source and a background surface brightness was defined using the average of 20 points evenly distributed throughout the annulus between the two circles. Flux values were calculated using the two apertures and compared. If there was a large discrepancy between the two values then the background surface brightness was too variable and the point source was rejected from the sample. Otherwise the average of the two fluxes was used in the comparison with the PSC. The results of the photometry are tabulated in Table 3 and average flux ratio and background values, along with the standard deviation about the average, are listed in Table 4.

Both wavelength bands experience the same general trend. There is an average 6% positive offset from the PSC at the first iteration and negative 4% offset after 20 iterations. This decrease in point-source flux with iteration is not a universal property of HIRES processing. Cao et al. (1997) report for the IGA, using a sample of 35 point sources, that at 60 μm, on average there are 12% and 14% offsets from the PSC after 1 and 20 iterations, respectively, and at 100 μm the offsets are 1% and 11%. In the IGA case part of the trend is thought to come from a systematic decrease in the background attributed to increased point-source ringing, and so one possible cause of the trend observed for the MIGA might be a systematic increase of the background level with increasing iterations. However, as shown in Table 4 the average background value actually

[6] Skyview is a general purpose FITS image viewing and analysis tool available at http://www.ipac.caltech.edu/Skyview/.

TABLE 3

MIGA PHOTOMETRY TEST

	PSC POSITION		PSC FLUX (Jy)		MIGA FLUX (Jy)			
IRAS	l	b	12 μm	25 μm	12 μm (1)	12 μm (20)	25 μm (1)	25 μm (20)
00067+6340.....	118.3409	1.4576	53.36	28.22	63.54	48.65	28.59	22.76
00186+5940.....	119.1762	−2.6994	24.51	10.14	25.78	25.08	10.08	10.97
00340+6251.....	121.3003	0.3074	50.41	19.37	47.03	42.33	19.10	17.02
00362+5924.....	121.3715	−3.1555	25.50	15.20	24.65	22.96	16.00	13.68
01071+6551.....	124.8524	3.3233	24.35	12.30	26.04	23.26	12.63	12.52
01142+6306.....	125.8542	0.6440	30.06	18.08	30.44	29.83	18.11	17.05
01145+5902.....	126.2820	−3.3949	21.64	10.30	25.96	22.30	12.08	10.36
01217+6049.....	126.9839	−1.5298	52.31	31.26	52.71	45.30	32.83	29.10
01261+6446.....	126.9464	2.4612	21.84	12.04	22.08	21.78	13.11	11.92
01364+6038.....	128.7872	−1.4185	17.41	10.25	17.07	15.08	9.89	10.90
01443+6417.....	128.9559	2.3395	49.95	18.87	50.00	45.83	19.78	17.60
01572+5844.....	131.7681	−2.6935	25.62	16.11	19.80	21.78	18.06	15.68
01577+6354.....	130.4745	2.3018	26.53	19.41	33.40	29.04	19.87	18.11
02044+6031.....	132.1572	−0.7257	12.05	105.8	14.29	13.12	115.18	106.66
02086+6355.....	131.6201	2.6685	29.37	17.32	30.08	26.43	16.58	16.21
02217+5712.....	135.3331	−3.1573	18.53	13.25	21.51	17.94	14.50	13.10
02347+5649.....	137.1203	−2.8495	38.85	26.12	37.76	38.15	26.59	24.34
02469+5646.....	138.6543	−2.2057	90.58	78.86	93.69	77.19	85.33	71.03
02473+5738.....	138.3201	−1.3976	39.04	26.45	47.16	38.34	33.53	28.18
03042+5850.....	139.7360	0.6994	22.62	13.02	22.09	18.85	13.94	12.35
03094+5530.....	142.0154	−1.8251	57.78	21.07	66.19	55.87	23.76	20.33
03301+5658.....	143.6405	0.9657	15.12	14.72	18.82	17.02	16.20	15.72
03385+5927.....	143.0775	3.6207	59.41	36.58	50.40	42.75	29.24	26.73
03419+5429.....	146.4398	−0.0588	15.53	12.64	14.72	12.02	12.62	12.20
20026+4018.....	76.4321	4.8081	23.98	11.34	23.78	22.14	12.44	11.78
20028+3910.....	75.4887	4.1759	41.78	210.8	45.33	42.77	224.88	185.30
20282+3604.....	75.7746	−1.7196	39.74	17.27	39.80	40.54	18.70	19.17
20422+4644.....	85.8464	2.6680	14.34	16.03	14.39	13.42	16.43	14.00
20499+4657.....	86.8478	1.7934	29.22	25.37	29.93	24.13	25.08	21.44
20502+4709.....	87.0338	1.8859	104.9	62.22	110.63	91.48	74.46	59.63
20549+5245.....	91.7978	4.9220	64.88	51.15	65.92	61.72	55.30	50.29
21015+4859.....	89.6478	1.6478	26.04	16.14	30.60	29.86	17.34	18.07
21122+4900.....	90.8629	0.3731	14.43	16.66	18.73	17.16	20.53	18.87
21167+5502.....	95.6773	4.0997	24.22	10.18	29.29	27.47	11.24	11.10
21223+5114.....	93.5840	0.8016	69.98	48.78	66.82	66.23	57.76	50.21
21232+5705.....	97.7603	4.9227	44.59	17.65	47.10	41.85	18.27	15.20
21282+5050.....	93.9862	−0.1185	50.99	74.36	57.27	41.66	77.56	62.04
21444+5053.....	95.9339	−1.7734	17.16	15.68	18.06	17.08	16.22	15.16
21453+5959.....	101.8655	5.1417	24.38	19.08	20.47	17.45	18.11	15.76
21475+5211.....	97.1263	−1.0757	22.89	13.41	25.43	24.98	15.44	15.89
22122+5745.....	103.3018	1.2718	32.19	17.73	37.81	32.92	19.78	19.67
22248+6058.....	106.3922	3.0933	12.04	12.19	12.38	11.66	13.77	13.30
22303+5950.....	106.3932	1.7784	54.46	68.41	61.33	48.03	71.68	62.26
22413+5929.....	107.4251	0.7972	58.52	28.41	55.79	59.00	28.20	27.62
22471+5902.....	107.8860	0.0507	19.04	14.47	18.22	16.93	14.31	14.51
22489+6359.....	110.2892	4.3798	46.38	22.28	46.44	37.44	21.79	17.80
23000+5932.....	109.5835	−0.1895	55.61	38.48	57.07	48.79	39.96	32.81
23106+6340.....	112.3522	3.1283	30.74	14.38	38.21	34.16	14.86	13.96
23239+5754.....	111.8786	−2.8500	20.86	71.22	23.87	24.26	72.33	72.48
23281+5742.....	112.3421	−3.2212	83.73	69.30	89.46	77.09	76.00	61.91
23321+6545.....	115.2069	4.3214	13.66	85.61	15.82	13.26	102.82	78.55
23592+6228.....	117.2816	0.4239	23.18	16.04	26.42	22.19	16.85	14.74

NOTE.—Galactic latitude and longitude (l, b) are given in degrees.

decreases very slightly. Also since we do not see this decrease occurring in every single point source tested (e.g., IRAS 20282+3604 or IRAS 23239+5754), it is not a universal property of the algorithm being used.

Since this behavior is different than that seen in the IGA, we compared a subset of 16 point sources processed using the ringing reduction algorithm and without (as for the IGA). The results are shown in Table 5 for the twentieth iteration images. The first iteration images are identical in both cases and were remeasured to gain an idea of the uncertainties involved in the photometric measuring technique being used. Differences in the measured fluxes were less than 0.1%; of course a more sophisticated photometry routine would reduce this uncertainty further. In general the fluxes measured without the ringing suppression algorithm in place are higher than the fluxes from the MIGA images.

TABLE 4

MIGA Photometry Test Average Results

Ratio	Mean	St. Dev.
12 μm Band		
MIGA(1)/PSC	1.06	0.11
MIGA(20)/PSC	0.95	0.11
MIGA(20)/MIGA(1)	0.90	0.076
Mean background (1)[a]	3.94	1.57
Mean background (20)[a]	3.89	1.57
25 μm Band		
MIGA(1)/PSC	1.06	0.080
MIGA(20)/PSC	0.96	0.096
MIGA(20)/MIGA(1)	0.91	0.078
Mean background (1)[a]	6.94	1.72
Mean background (20)[a]	6.87	1.70

[a] Background units are MJy sr^{-1}

Average results for this test are shown in Table 6. Without the ringing suppression algorithm the point source flux tends to increase as the iterations increase, like the IGA though less dramatically, whereas with the algorithm in place the point source flux tends to decrease with increasing iterations as before. However, this behavior is not found for every single source; if the point source flux does increase for a MIGA source, then it tends to increase less than it does when the ringing suppression algorithm is not used, thus preserving the sense of the relative behavior.

While the photometry obtained without the ringing suppression algorithm in place tends to match the PSC flux values better, we decided that the possible benefits of having the ringing suppression algorithm in place outweighed the slightly worse (but still comparing well to the IGA) photometric performance. Furthermore, as discussed in § 4.5 there are other sources of error in flux measurement that will tend to swamp this uncertainty.

4.4. *Size-Dependent Flux Calibration*

One quirk of the *IRAS* detectors was that their sensitivity was a function of the dwell-time of a source: the so-called AC/DC effect. Due to this behavior two calibrations for *IRAS* data were developed. The AC calibration, used for the MIGA and IGA, is suitable for point sources. The DC calibration is suitable for measuring fluxes from extended emission more than 2° in extent (Wheelock et al. 1994). For structure at intermediate scales (6′–2°) well-defined conversion factors exist for the mid-infrared *IRAS* bands and users should consult Table II.B.1 in Wheelock et al. (1994).

In order to convert MIGA data to the DC scale, images need to be multiplied by 0.78 and 0.82 at 12 and 25 μm, respectively. Unlike the 60 and 100 μm bands, where the correction depends upon the strength of the source (especially for very bright extended emission), the AC/DC correction for the mid-infrared *IRAS* bands appears to be more stable and does not appear to have any dependence on the source brightness (*IRAS* Explanatory Supplement 1988).

TABLE 5

Ringing Suppression Photometry Test at Iteration 20

	12 μm Flux (Jy)		25 μm Flux (Jy)	
IRAS	MIGA	WRS	MIGA	WRS
00186+5940	25.08	26.44	10.97	11.12
00340+6251	42.33	50.78	17.02	19.83
01142+6306	29.83	36.03	17.05	19.52
01572+5844	21.78	24.74	15.68	19.79
01577+6354	29.04	32.45	18.11	18.82
02086+6355	26.43	32.33	16.21	17.86
02469+5646	77.19	92.38	71.03	84.16
03385+5927	42.75	48.43	26.73	32.36
20028+3910	42.77	45.62	185.30	220.08
20499+4657	24.13	27.49	21.44	24.24
20502+4709	91.48	115.01	59.63	75.24
20549+5245	61.72	67.78	50.29	56.30
21444+5053	17.08	18.56	15.16	15.83
22413+5929	59.00	60.10	27.62	29.41
23000+5932	48.79	60.87	32.81	41.64
23281+5742	77.09	93.18	61.91	80.36

Note.—WRS: without ringing suppression.

TABLE 6

Ringing Suppression Photometry Test—Average Results

Ratio	Mean	St. Dev.
12 μm Band		
MIGA(1)/PSC	1.01	0.106
MIGA(20)/PSC	0.92	0.097
MIGA(20)/MIGA(1)	0.91	0.084
WRS(1)/PSC	1.01	0.105
WRS(20)/PSC	1.06	0.098
WRS(20)/WRS(1)	1.05	0.082
25 μm Band		
MIGA(1)/PSC	1.03	0.087
MIGA(20)/PSC	0.92	0.078
MIGA(20)/MIGA(1)	0.90	0.077
WRS(1)/PSC	1.03	0.087
WRS(20)/PSC	1.06	0.089
WRS(20)/WRS(1)	1.03	0.049

Note.—WRS: without ringing suppression.

4.5. *Flux and Surface Brightness Measurement Uncertainty*

Section 2.3 of Fich & Terebey (1996) gives a good general discussion of the variety of factors involved in estimating uncertainties in *IRAS* flux measurements, including instrumental, choice of measurement technique, and background effects and is recommended reading for users of both the MIGA and IGA. It is clear that actual uncertainties in measured point source flux values from the MIGA will be much higher than the basic uncertainty of $\lesssim 6\%$ implied by the photometric tests against the PSC discussed in § 4.3. Due to complex background emission, uncertainties in flux measurements can reach as high as 44% and 20% at 12 and 25 μm, respectively. Instrumental uncertainties in the mid-infrared *IRAS* data are smaller than uncertainties caused by uncertain background estimation and/or different measurement techniques. As mentioned in § 4.4, the AC/DC effect, although larger than at far-infrared wavelengths, is well behaved.

Like for the IGA, the ISSA was used as a large scale surface brightness truth table for the MIGA. In order to check this calibration we selected five MIGA images from across the atlas region. The images were reprojected and rebinned to the geometry and pixel size of the ISSA and

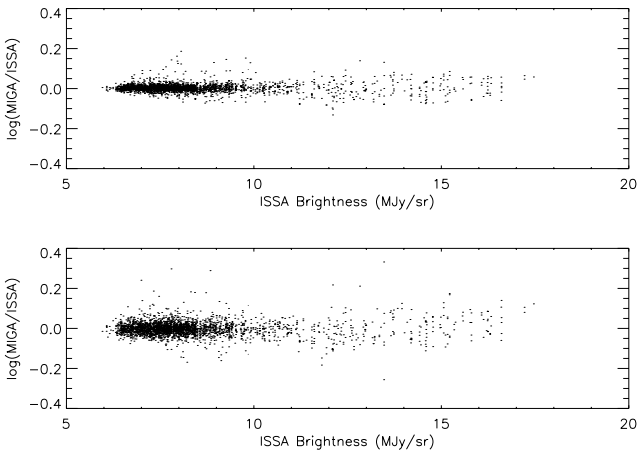

FIG. 7.—Data from the surface brightness test for the 12 μm MIGA image at $l = 75°$, $b = 2°.0$. Top panel shows iteration 1, bottom panel shows iteration 20.

compared pixel-by-pixel with the respective ISSA plate. The ISSA plates were first divided by 0.78 and 0.82 (at 12 and 25 μm, respectively) in order to convert them to the AC calibration. The results of the test are tabulated in Table 7, and data for one of the test areas are plotted in Figure 7.

Any uncertainties inherent to the ISSA can be passed along to the MIGA. Of most concern is the uncertainty in the zodiacal light model that was subtracted from the ISSA since this dominates the uncertainty of the absolute zero point at 12 and 25 μm (Wheelock et al. 1994). Residual zodiacal light removal errors are 3%–5% of the original emission (0.5 MJy sr^{-1} at 12 μm and 1.0 MJy sr^{-1} at 25 μm) for $\beta > 50°$ and are 1.0 MJy sr^{-1} at 12 μm and 2.0–2.5 MJy sr^{-1} over scales of 10° for $50° > \beta > 20°$ (Wheelock et al. 1994). Most of the MIGA coverage is at high ecliptic latitude, and so these residual errors will be minimal.

To illustrate this uncertainty we compared the average surface brightness of the five MIGA images used in the ISSA comparison to the Diffuse Infrared Background Experiment (DIRBE) Zodiacal Subtracted Mission Average maps (ZSMA).[7] DIRBE measurements are the best-calibrated data available on the mid-infrared sky brightness on large spatial scales. For each region we first determined which ZSMA pixels fell entirely within each MIGA image (typically 9–12 $\sim 0°.32$ square pixels) and measured their average value. Then, after the MIGA images were converted to the DC scale, the surface brightness in regions on the MIGA images corresponding to the ZSMA pixels was determined and their average value was calculated. The results are shown in Table 7. At both 12 and 25 μm the relative surface brightness between different regions is approximately the same for both the MIGA and ZSMA. There is an offset between the MIGA and the ZSMA values, especially at 25 μm where the zodiacal light emission is the strongest, primarily due to uncertainties in the different zodiacal light models that were applied. As expected these residual zodiacal light errors are on the order of a few MJy sr^{-1}. As emphasized in the ISSA Explanatory Supplement, and demonstrated here, data products that are based upon the ISSA surface brightness scale (ISSA, MIGA, and IGA) should not be used to determine absolute sky surface brightness (Wheelock et al. 1994).

4.6. *Positional Accuracy*

We tested the positional accuracy of the MIGA against the PSC using the same point sources as for the photometry test. Using the IPAC Skyview program a 5′ radius circle was drawn around the position of the point source as given in the PSC (which is a weighted average of the position at each wavelength), and the flux-weighted centroid was then

[7] *COBE* Diffuse Infrared Background Experiment (DIRBE) Explanatory Supplement, Version 2.1. 1997, ed. M. G. Hauser, T. Kelsall, D. Leisawitz, & J. Weiland (*COBE* Ref. Pub. 97-A; Greenbelt: NASA/GSFC), available in electronic form from the NSSDC at http://www.gsfc.nasa.gov/astro/cobe/

TABLE 7

SURFACE BRIGHTNESS TESTS

IMAGE	ITERATION 1		ITERATION 20		ZSMA (MJy sr^{-1})[c]		MIGA (MJy sr^{-1})[d]	
	$\log\left(\frac{\text{MIGA}}{\text{ISSA}}\right)$[a]	σ[b]	$\log\left(\frac{\text{MIGA}}{\text{ISSA}}\right)$	σ		σ		σ
12 μm Band								
g075+02[e]	0.0029	0.02	0.00021	0.04	4.9	0.5	6.4	1.0
g086+05	0.0030	0.02	0.00054	0.04	3.1	0.4	3.7	0.6
g102−03	0.0032	0.03	−0.0047	0.09	1.5	0.1	1.3	0.2
g120−01	0.0031	0.02	−0.0019	0.06	2.4	0.4	2.3	0.5
g141−02	0.0037	0.05	−0.0038	0.09	3.3	0.6	3.0	0.5
25 μm Band								
g075+02	0.0017	0.02	−0.00077	0.03	6.3	0.6	10.	1.
g086+05	0.0011	0.007	0.00055	0.02	4.2	0.5	7.0	0.6
g102−03	0.00043	0.007	−0.00010	0.02	2.2	0.1	4.1	0.2
g120−01	0.00058	0.01	−0.00044	0.02	3.2	0.5	5.8	0.6
g141−02	0.0018	0.03	−0.0023	0.06	4.2	0.6	5.7	0.6

[a] Average over image.
[b] Standard deviation of the mean.
[c] Average of ZSMA pixels within MIGA image; ZSMA = Zodi-Subtracted Mission Average maps.
[d] Average brightness of regions corresponding to ZSMA pixels; iteration 20 image.
[e] See Fig. 7 for MIGA − ISSA comparison data.

measured for the pixels within the circle. This value was taken as the position of the point source from the MIGA.

The results of this test are shown in Table 8. At 12 μm the average measured distance from the PSC position was 7.″88 $\pm$ 4.″0 (± 1 σ scatter) and at 25 μm was 6.″69 $\pm$ 3.″2. The positional accuracy of the MIGA is similar to that reported for the IGA: 7.″6 $\pm$ 5.″6 at 60 μm and 7.″1 $\pm$ 4.″1 at 100 μm. The position angle of the offset is different for the 12 and 25 μm point sources, but no systematic trend was found. The position angle differences are most likely due to a combination of the differences in the detailed beam shape and the background in each band, which causes the flux-weighted centroid of the aperture to shift slightly between each band.

TABLE 8

POSITION TEST RESULTS

	PSC POSITION		MIGA 12 μm		MIGA 25 μm		DISTANCE[a] (arcsec)	
IRAS	l	b	l	b	l	b	12 μm	25 μm
00067+6340.....	118.3409	1.4576	118.3385	1.4589	118.3388	1.4592	9.8	9.4
00186+5940.....	119.1762	−2.6994	119.1747	−2.6980	119.1747	−2.6991	7.5	5.5
00340+6251.....	121.3003	0.3074	121.2981	0.3073	121.3002	0.3068	7.9	2.1
00362+5924.....	121.3715	−3.1555	121.3704	−3.1534	121.3690	−3.1559	8.7	9.2
01071+6551.....	124.8524	3.3233	124.8476	3.3210	124.8492	3.3244	19.1	12.1
01142+6306.....	125.8542	0.6440	125.8532	0.6449	125.8546	0.6457	4.8	6.3
01145+5902.....	126.2820	−3.3949	126.2779	−3.3938	126.2792	−3.3930	15.3	12.1
01217+6049.....	126.9839	−1.5298	126.9852	−1.5254	126.9828	−1.5302	16.5	4.3
01261+6446.....	126.9464	2.4612	126.9441	2.4625	126.9438	2.4614	9.4	9.5
01364+6038.....	128.7872	−1.4185	128.7854	−1.4179	128.7853	−1.4181	6.8	6.8
01443+6417.....	128.9559	2.3395	128.9548	2.3420	128.9536	2.3393	9.8	8.3
01572+5844.....	131.7681	−2.6935	131.7683	−2.6912	131.7693	−2.6929	8.2	4.8
01577+6354.....	130.4745	2.3018	130.4735	2.3016	130.4735	2.3009	3.7	5.0
02044+6031.....	132.1572	−0.7257	132.1547	−0.7247	132.1546	−0.7247	9.0	9.9
02086+6355.....	131.6201	2.6685	131.6179	2.6697	131.6190	2.6700	9.0	6.8
02217+5712.....	135.3331	−3.1573	135.3341	−3.1529	135.3346	−3.1542	16.3	12.4
02347+5649.....	137.1203	−2.8495	137.1191	−2.8463	137.1183	−2.8496	12.0	7.1
02469+5646.....	138.6543	−2.2057	138.6546	−2.2044	138.6530	−2.2062	4.7	5.0
02473+5738.....	138.3201	−1.3976	138.3203	−1.3972	138.3199	−1.3979	1.5	1.4
03042+5850.....	139.7360	0.6994	139.7346	0.6992	139.7353	0.6997	5.0	2.7
03094+5530.....	142.0154	−1.8251	142.0152	−1.8255	142.0154	−1.8242	1.7	3.0
03301+5658.....	143.6405	0.9657	143.6404	0.9654	143.6407	0.9654	1.1	1.5
03385+5927.....	143.0775	3.6207	143.0759	3.6185	143.0748	3.6183	9.8	13.1
03419+5429.....	146.4398	−0.0588	146.440	−0.0599	146.4395	−0.0600	4.1	4.5
20026+4018.....	76.4321	4.8081	76.4300	4.8086	76.4287	4.8091	7.9	12.9
20028+3910.....	75.4887	4.1759	75.4913	4.1728	75.4902	4.1753	14.4	6.0
20282+3604.....	75.7746	−1.7196	75.7742	−1.7170	75.7753	−1.7180	9.5	6.3
20422+4644.....	85.8464	2.6680	85.8437	2.6695	85.8440	2.6699	11.3	11.0
20499+4657.....	86.8478	1.7934	86.8484	1.7952	86.8488	1.7946	6.9	5.6
20502+4709.....	87.0338	1.8859	87.0340	1.8871	87.0341	1.8863	4.3	2.0
20549+5245.....	91.7978	4.9220	91.7979	4.9231	91.7982	4.9223	4.1	1.7
21015+4859.....	89.6478	1.6478	89.6496	1.6493	89.6496	1.6493	8.6	8.6
21122+4900.....	90.8629	0.3731	90.8645	0.3739	90.8646	0.3747	6.4	8.4
21167+5502.....	95.6773	4.0997	95.6749	4.1001	95.6751	4.1000	8.6	8.1
21223+5114.....	93.5840	0.8016	93.5831	0.8018	93.5840	0.8008	3.2	3.0
21232+5705.....	97.7603	4.9227	97.7609	4.9253	97.7593	4.9235	9.6	4.4
21282+5050.....	93.9862	−0.1185	93.9863	−0.1172	93.9863	−0.1171	4.6	5.1
21444+5053.....	95.9339	−1.7734	95.9345	−1.7744	95.9345	−1.7744	4.3	4.2
21453+5959.....	101.8655	5.1417	101.8635	5.1409	101.8645	5.1410	7.7	4.5
21475+5211.....	97.1263	−1.0757	97.1246	−1.0742	97.1242	−1.0748	8.0	8.2
22122+5745.....	103.3018	1.2718	103.3008	1.2722	103.3008	1.2712	3.8	4.1
22248+6058.....	106.3922	3.0933	106.3902	3.0953	106.3914	3.0958	10.3	9.4
22303+5950.....	106.3932	1.7784	106.3917	1.7798	106.3931	1.7813	7.5	10.4
22413+5929.....	107.4251	0.7972	107.4241	0.7970	107.4248	0.7958	3.5	5.3
22471+5902.....	107.8860	0.0507	107.8863	0.0503	107.8851	0.0503	1.8	3.6
22489+6359.....	110.2892	4.3798	110.2887	4.3810	110.2893	4.3815	4.7	6.3
23000+5932.....	109.5835	−0.1895	109.5848	−0.1874	109.5842	−0.1886	8.8	4.3
23106+6340.....	112.3522	3.1283	112.3498	3.1283	112.3503	3.1292	8.5	7.5
23239+5754.....	111.8786	−2.8500	111.8772	−2.8486	111.8763	−2.8496	7.1	8.4
23281+5742.....	112.3421	−3.2212	112.3382	−3.2207	112.3401	−3.2186	14.2	11.6
23321+6545.....	115.2069	4.3214	115.2051	4.3203	115.2052	4.3221	7.7	6.6
23592+6228.....	117.2816	0.4239	117.2787	0.4240	117.2799	0.4252	10.5	7.7

NOTE.—Galactic latitude and longitude (l, b) are given in degrees.

[a] Absolute offset between MIGA and PSC position at each wavelength.

TABLE 9

POSITION TEST—15″ PIXELS[a]

	PSC POSITION		12 μm		25 μm		DISTANCE (arcsec)	
IRAS	l	b	l	b	l	b	12 μm	25 μm
02570+5844.....	138.9591	0.1584	138.9584	0.1577	138.9584	0.1576	4.7	5.0
02568+5931.....	138.5898	0.8357	138.5795	0.8379	138.5791	0.8375	8.1	7.2
03012+5942.....	138.9766	1.2617	138.9757	1.2628	138.9753	1.2625	4.4	6.5
02552+5937.....	138.3453	0.8277	138.3444	0.8299	138.3451	0.8293	9.2	6.0
02504+5917.....	137.9660	0.2526	137.9648	0.2542	137.9653	0.2544	6.7	7.6
02474+5901.....	137.7270	−0.1555	137.7271	−0.1526	137.7254	−0.1543	10.4	8.4
02515+6001.....	137.7552	0.9805	137.7538	0.9794	137.7543	0.9801	5.8	4.6
02401+5923.....	136.7289	−0.2174	136.7281	−0.2167	136.7290	−0.2165	4.1	3.2
02368+5955.....	136.1374	0.0901	136.1370	0.0912	136.1369	0.0913	4.1	4.7
02314+5942.....	135.5906	−0.3742	135.5890	−0.3741	135.5914	−0.3743	5.8	1.4
02355+6029.....	135.7592	0.5560	135.7581	0.5528	135.7581	0.5538	12.4	8.9

[a] Regular MIGA pixel size.

To investigate what effect rebinning the MIGA to produce CGPS mosaics with 18″ pixels has on the positional accuracy we repeated the test on 11 point sources in the W5 region. The results are shown in Table 9 and Table 10. Both the original MIGA and the CGPS mosaicked MIGA are in close agreement, with the original MIGA agreeing only slightly better with the point source catalog positions. At 12 μm the average distance from the PSC positions was 6.″89 ± 2.″8 with 15″ pixels and 7.″32 ± 4.″0 with 18″ pixels. At 25 μm the average distance from the PSC positions was 5.″76 ± 2.″3 and 6.″57 ± 3.″5 with 15″ pixels and 18″ pixels, respectively.

4.7. *Mosaic Property*

The large angular scale preprocessing of the *IRAS* data allows large high-quality mosaics to be constructed from the final HIRES images. In order to quantify the quality of the mosaics, which tend to be seamless to the eye, we tested

TABLE 10

POSITION TEST—18″ PIXELS[a]

	PSC POSITION		12 μm		25 μm		DISTANCE (arcsec)	
IRAS	l	b	l	b	l	b	12 μm	25 μm
02570+5844.....	138.9591	0.1584	138.9599	0.1592	138.9600	0.1592	4.3	4.3
02568+5931.....	138.5798	0.8357	138.5803	0.8355	138.5799	0.8351	0.9	2.3
03012+5942.....	138.9766	1.2617	138.9756	1.2604	138.9754	1.2600	5.2	8.3
02552+5937.....	138.3453	0.8277	138.3436	0.8307	138.3443	0.8302	11.6	10.0
02504+5917.....	137.9660	0.2526	137.9633	0.2550	137.9636	0.2553	13.7	12.0
02474+5901.....	137.7270	−0.1555	137.7272	−0.1534	137.725	−0.1551	7.9	7.3
02515+6001.....	137.7552	0.9805	137.7552	0.9802	137.7554	0.9809	1.4	1.8
02401+5923.....	136.7289	−0.2174	136.7287	−0.2153	136.7298	−0.2150	7.7	9.6
02368+5955.....	136.1374	0.0901	136.1349	0.0898	136.1345	0.0898	8.7	8.7
02314+5942.....	135.5906	−0.3742	135.5875	−0.3740	135.5898	−0.3742	9.4	2.2
02355+6029.....	135.7592	0.5560	135.7596	0.5535	135.7598	0.5546	9.6	5.7

[a] CGPS mosaic pixel size.

TABLE 11

MOSAIC TEST RESULTS—12 μm

	FIRST ITERATION		TWENTIETH ITERATION	
PLATE	Mean Ratio − 1 (%)	St. Dev. (%)[a]	Mean Ratio − 1 (%)	St. Dev. (%)
p1572.....	−0.13	0.49	−0.07	3.19
p1573.....	−0.08	0.32	−0.13	2.00
p1574.....	0.06	0.48	0.09	1.50
p1575.....	0.09	0.30	0.13	1.78
Combined[b].....	−0.02	0.42	0.00	2.24
Edges[c].....	−0.08	1.24	−0.03	5.46

[a] Standard deviation from pixel ratio values are reported as a measure of the scatter.
[b] Total of 32294 pixels within the plates.
[c] Total of 4579 pixels along plate edges.

TABLE 12

MOSAIC TEST RESULTS—25 μm

PLATE	FIRST ITERATION		TWENTIETH ITERATION	
	Mean Ratio − 1 (%)	St. Dev. (%)[a]	Mean Ratio − 1 (%)	St. Dev. (%)
p1572	−0.07	0.22	−0.09	1.05
p1573	−0.08	0.25	−0.04	1.03
p1574	0.01	0.29	−0.01	0.65
p1575	0.06	0.14	0.05	0.63
Combined[b]	−0.02	0.24	−0.02	0.87
Edges[c]	−0.03	0.67	−0.03	2.05

[a] Standard deviation of pixel ratio values are reported as a measure of the scatter.
[b] Total of 32294 pixels within the plates.
[c] Total of 4579 pixels along plate edges.

the mosaic property using data from four CRDD plates. This allowed us to study 134 boundaries between images within the plates and 19 boundaries across plates. The latter are expected to be worse because they were preprocessed completely separately.

TABLE 13

MIGA AND IGA MOSAIC TEST COMPARISON[a]

WAVELENGTH (μm)	INTERNAL ST. DEV. (%)		EDGE ST. DEV. (%)	
	Iteration 1	Iteration 20	Iteration 1	Iteration 20
100	0.08	0.23	0.18	0.46
60	0.14	0.51	0.52	1.5
25	0.24	0.87	0.67	2.1
12	0.42	2.2	1.2	5.5

[a] Different plates were used for the IGA and MIGA tests.

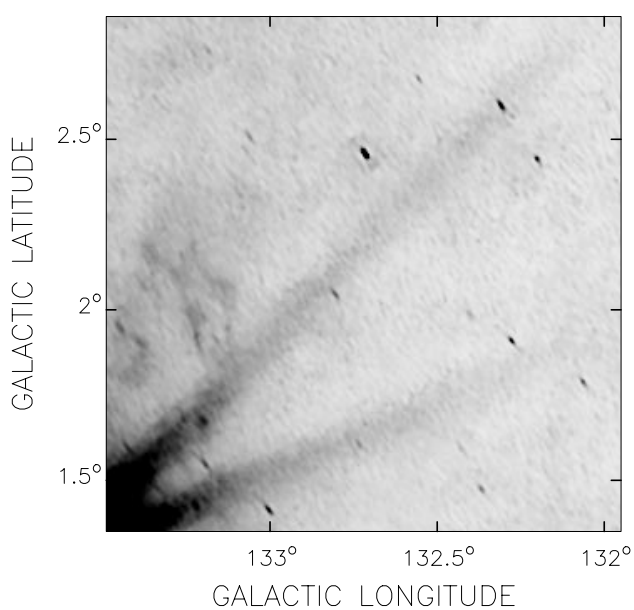

FIG. 8.—Spectacular demonstration of multiple point source tails from detector hysteresis. This 12 μm MIGA mosaic shows two tails extending from the extremely bright W3 region in the lower left corner of the image. The image is linearly stretched between 4.44 MJy sr^{-1} (*white*) and 15.0 MJy sr^{-1} (*black*). The offset between the brightness of the tails and the area outside of them is $\sim$1 MJy sr^{-1} over most of the length of the tail. Two tails are present because of the two noticeably different scan directions of the *IRAS* satellite in this region.

The tests were done by comparing the pixels along a 1 pixel wide strip, 1° long, that is common between adjoining images. A total of 32,294 pixels was examined along boundaries contained entirely within a single CRDD plate, and 4579 pixels were examined in the cross-CRDD test.

The pixel ratios (−1) and the standard deviations are tabulated in Tables 11 and 12 for the 12 and 25 μm data, respectively. In Table 13 the standard deviations are shown again along with data from the IGA, showing that the mosaic quality decreases as one moves toward shorter wavelengths. This is caused by a combination of increasing resolution and more complex backgrounds making the images less smooth as one moves into the mid-infrared.

4.8. *Residual Hysteresis*

IRAS detectors experience a hysteresis effect after passing over a bright source. While the Galactic plane shadowing effect described by Cao et al. (1997) for the IGA does not affect the 12 and 25 μm detectors, hysteresis also can cause bright point sources to have tails associated with them. Although this can occur at any wavelength, it is most prominent at 12 and 25 μm for point sources brighter than 15–20 Jy (Wheelock et al. 1994). As shown in Figure 8, a single source can have a number of tails, one for each scan direction. Clearly, this effect can cause difficulties in the interpretation of structure near bright point sources, and additional care must be taken even when doing photometry of bright point sources.

5. ARTIFACTS

In the following paragraphs we will discuss briefly various processing artifacts, namely stripes, glitches, coverage artifacts, and discontinuities, of which users of the MIGA should be aware. Since the processing of the MIGA closely followed that of the IGA, we refer the reader to Cao et al. (1997) for a detailed discussion. The effect of a new ringing suppression algorithm is treated in § 5.1.

The MIGA used the same destriping technique as in the IGA. Stripes, which were once the most common artifact in images constructed from *IRAS* data, are now almost completely eliminated from HIRES images. Details on the destriping algorithm and the application to the IGA can be found in Cao et al. (1996) and Cao et al. (1997).

A glitch is the term given to a cosmic-ray or trapped energetic particle hit on the *IRAS* detectors that shows up in the *IRAS* data stream. As with the IGA, the LAUNDR

TABLE 14

RINGING SUPPRESSION ALGORITHM—SURFACE BRIGHTNESS TEST

l	b	log (MIGA/ISSA)	St. Dev.	log (WRS[a] /ISSA)	St. Dev.
142.2.....	−1.52	−0.0015	0.034	−0.0018	0.034
142.4.....	−1.95	0.0001	0.034	−0.0001	0.034
142.2.....	−2.41	−0.0033	0.037	−0.0039	0.036
141.5.....	−2.43	−0.0026	0.035	−0.0024	0.034
141.5.....	−1.81	−0.0028	0.036	−0.0029	0.036

NOTE.—Coordinates are for the center of 10′ radius apertures.
[a] WRS: no ringing suppression applied.

preprocessing program was used to flag and remove most of the glitches. It is possible that some glitches did slip through this stage of the processing although none have been identified so far. For an example of a glitch artifact in the IGA see Figure 12 of Cao et al. (1997), glitches in the MIGA (and EIGA) would have the same properties.

Regions of low *IRAS* detector coverage can cause spurious structure to appear in HIRES images. Low coverage

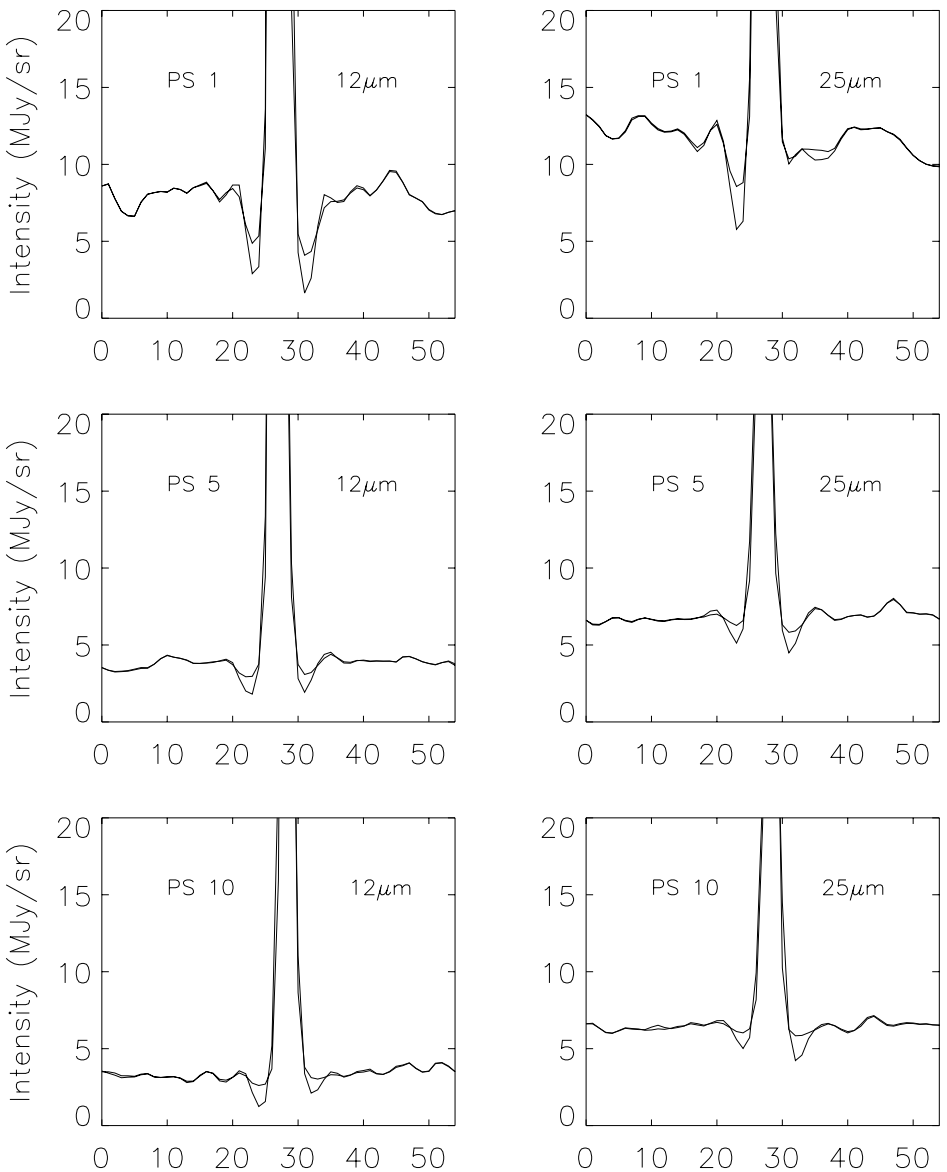

FIG. 9.—Illustration of the point source ringing suppression algorithm for three of the observed point sources at 12 and 25 μm (*left and right panels, respectively*). The figures show cuts taken across the center of the point source after processing with and without the algorithm. For simplicity, cuts were taken at constant Galactic latitude and thus the angle between the cut, and the minor axis of the point source and the scan direction(s) is variable. In all cases the algorithm led to a reduction in the amount of ringing around the point source, and so the deeper troughs are associated with processing without the algorithm. The peak 12 μm intensities, without the ringing suppression algorithm, are 308, 105, and 59 MJy sr^{-1} for point sources 1, 5, and 10, respectively. At 25 μm, without ringing suppression, the peak intensities are 86, 41, and 37 MJy sr^{-1}, respectively. The amount of ringing depends on the peak intensity (see text for details).

TABLE 15

DEPTH OF POINT SOURCE RINGING

SOURCE	IRAS	FLUX (Jy)		DEPTH (MIGA)/DEPTH (WRS)[a]			
		12 μm	25 μm	12 μm Left[b]	12 μm Right[c]	25 μm Left	25 μm Right
1	02459+6049	16.66	5.16	0.74	0.66	0.58	0.72
2	02445+6042	5.85	10.94	0.69	0.49	0.60	0.04
3	02455+6130	5.40	1.68	0.33	0.52	0.44	0.63
4	02358+5928	11.27	4.90	0.45	0.29	0.06	0.33
5	02368+5955	4.75	2.33	0.47	0.45	0.26	0.57
6	02399+6012	3.00	0.86	0.66	0.43	0.55	0.43
7	02391+5959	1.01	0.32	0.64	0.49	0.90	0.42
8	02474+5901	6.96	2.15	0.38	0.03	0.28	0.29
9	02504+5917	4.60	1.35	0.28	0.88	0.48	0.80
10.....	02401+5923	3.83	2.17	0.29	0.55	0.30	0.32

[a] Without ringing suppression.
[b] Refers to troughs on the left hand side of the point sources in Fig. 9.
[c] Refers to troughs on the right hand side of the point sources in Fig. 9.

or a steep gradient in the coverage can also cause point source positions to shift. Users of any HIRES product can use the coverage maps (cvg_*, see Table 1 and Fig. 2) to help determine if observed features could be affected or even caused by regions of low coverage.

Discontinuities can occasionally exist entirely within a MIGA image or mosaic as opposed to across image boundaries. These discontinuities trace their origin to the preprocessing step involving the ISSA images (for calibration and zodiacal emission removal). ISSA data are required corresponding to the geometry of the input CRDD plate, and so mosaics of ISSA images were constructed if necessary. Care was taken to minimize the discontinuities between ISSA images, but in some cases a small (on the order of 1 MJy sr^{-1}) discontinuity was unavoidable. This type of discontinuity is usually not visible in the first iteration image but is sharpened by the HIRES algorithm and becomes visible in the twentieth iteration image. An example of this type of discontinuity is given in Figure 13 of Cao et al. (1997).

5.1. *Ringing*

We were able to apply a ringing suppression algorithm based on Burg entropy minimization (Cao et al. 1999) to the MIGA data. Ringing is still visible around point sources but the level of the ringing is significantly reduced. Comparison between images constructed with and without the algorithm showed little difference in their global properties. For example, Table 14 shows results from a surface brightness accuracy test like the tests vs. ISSA presented in § 4.5. In this case we examined five different 10′ radius circular apertures at different locations across a 12 μm image. Since these tests showed that the images are virtually indistinguishable from regularly processed HIRES images away from point sources, the point source photometry tests in § 4.3 were acceptable (see Tables 5 and 6), and the algorithm had been shown to be useful in at least one published study (Noriega-Crespo et al. 1997), the ringing suppression algorithm was adopted for MIGA processing.

To quantify the beneficial effect of the ringing suppression algorithm on point sources in MIGA we processed five regions without the ringing suppression algorithm on (WRS) and selected 10 well-defined, isolated point sources. Cuts were then taken across the point sources, and the depth of the ringing on either side of each source was measured relative to the local background on either side. The change in the depth of the ringing was then calculated. The effect of the algorithm is generally to reduce the depth of the rings in every case. Figure 9 illustrates the effect of the algorithm on three of the point sources at 12 and 25 μm. There is also an increase the peak brightness (not shown). Note the excellent agreement between the two images as one moves away from the rings.

We found that as the flux of the point source increases the ringing tends to become more severe, as might be expected. At the same time the absolute value of the change in the ring depth also increases for stronger point sources. The result is that the fractional reduction in the ringing does not exhibit any trend with point source flux. The results of this calculation, along with data on the point source fluxes, are summarized in Table 15. For the point sources examined, the average value of ring depth (MIGA/WRS) was 0.49 ± 0.2 ($\pm 1\,\sigma$ scatter) and 0.45 ± 0.2 at 12 and 25 μm, respectively.

6. SAMPLE IMAGES

In this section we display a number of images from MIGA and the CGPS mosaic version of the MIGA in order to give readers an example of the data quality. Color versions of the images along with other samples are available on the web[8].

Figure 10 contrasts 12 and 25 μm images from ISSA and the corresponding images from MIGA. The improvement in the data quality is obvious.

Figure 11 shows a $4^\circ \times 3^\circ$ mosaic of the W5 region at 12 and 25 μm. This mosaic of 12 MIGA images can be constructed rapidly since the only operation required on the images is that they be trimmed before being mosaicked together; no reprojection step is required.

On larger scales Figure 12 shows one of the CGPS region mosaics. The great usefulness of the CGPS data format is that radio and millimeter data will be available for the same region at the same geometry and pixel size, greatly facilitating multiwavelength analysis of objects.

7. SUMMARY AND FUTURE DIRECTIONS

Currently, the MIGA covers the CGPS region in longitude and thus provides a mid-infrared data set for this

[8] http://www.ras.ucalgary.ca/CGPS/.

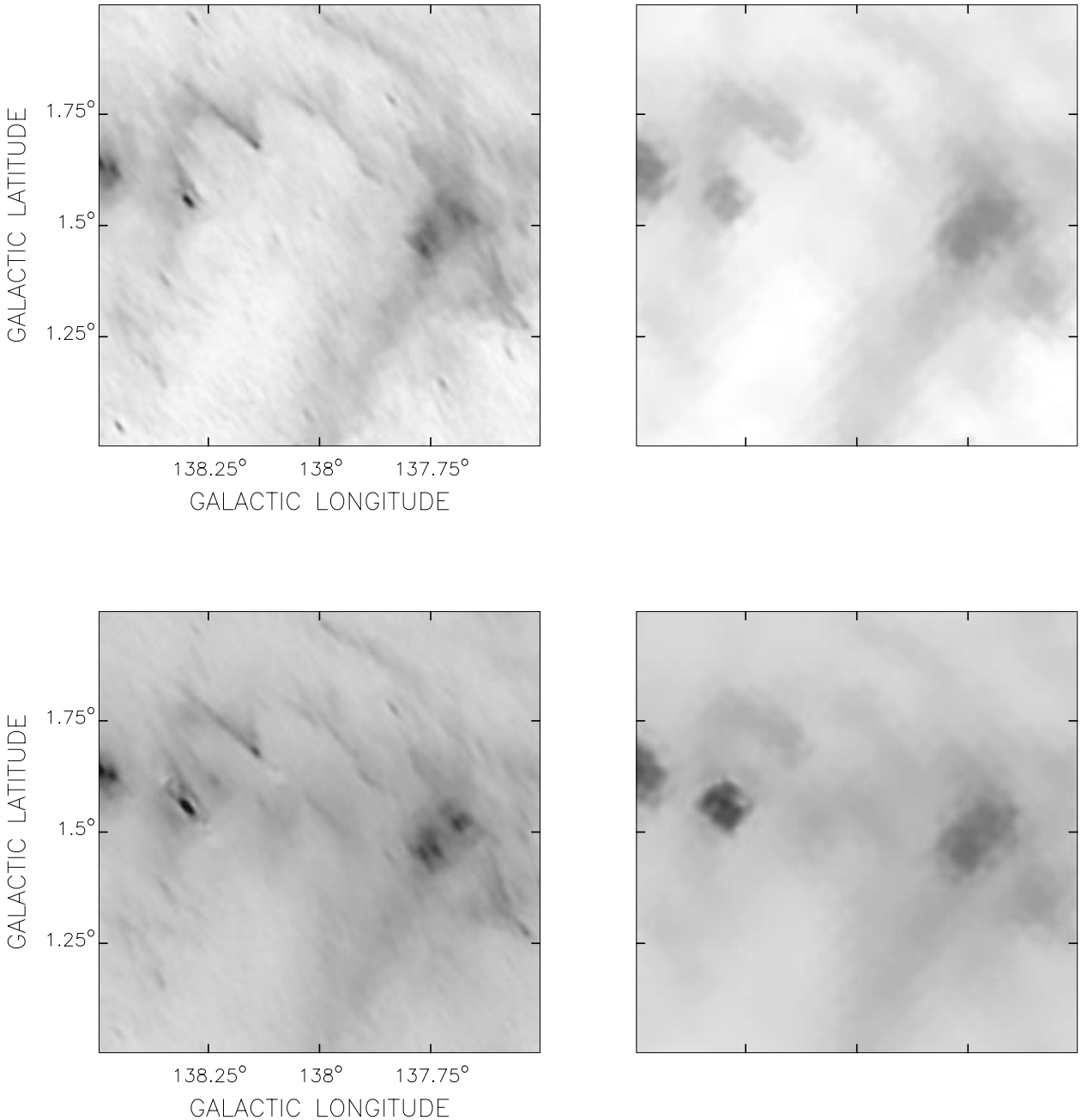

FIG. 10.—Comparison of ISSA and MIGA images showing mid-infrared emission associated with the H II region W5-East (*top*, 12 μm; *bottom*, 25 μm). The MIGA images, on the left, were cropped from MIGA mosaics made for Fig. 11. At 12 μm most of the emission is associated with the edges of molecular clouds surrounding the central ionized region. At 25 μm emission also extends into the ionized region. Both sets of images have the same logarithmic stretch from 3.0 to 700 MJy sr^{-1} (*white to black*).

multiwavelength survey. We considered continuing the MIGA processing to encompass more of the Galactic plane; however, in the future it is expected that mid-infrared data from the Mid-Course Space Experiment (MSX; Price 1995) will be made available for the entire Galactic plane ($\pm 5°$). Since this data set has a higher resolution (18″) than is possible to achieve using HIRES, we decided to focus further expansion of the MIGA to higher and lower Galactic latitudes in certain key areas tied to expansion of the CGPS. The CGPS is expected to enter a second phase of operation starting in 2000, where the focus will be on disk-halo interaction and extending the latitude coverage around Cygnus X and the Cepheus star forming region. In order to study the disk-halo interaction in our Galaxy effectively obviously one needs to be able to explore areas above the Galactic plane beyond $\pm 6°$. This has been clearly demonstrated through investigations of a possible chimney structure in W4 (Normandeau, Taylor, & Dewdney 1996; Basu, Johnstone, & Martin 1999) and unusual vertical H I structures (English et al. 1998b) that are analogous to H I "worms" (Heiles 1984).

The MIGA and IGA are flexible enough that new images can be attached seamlessly to existing images due to their being based on an all-sky survey and the processing technique. In Figure 13 we illustrate the addition of the EIGA images to the original IGA. This is a nice demonstration of

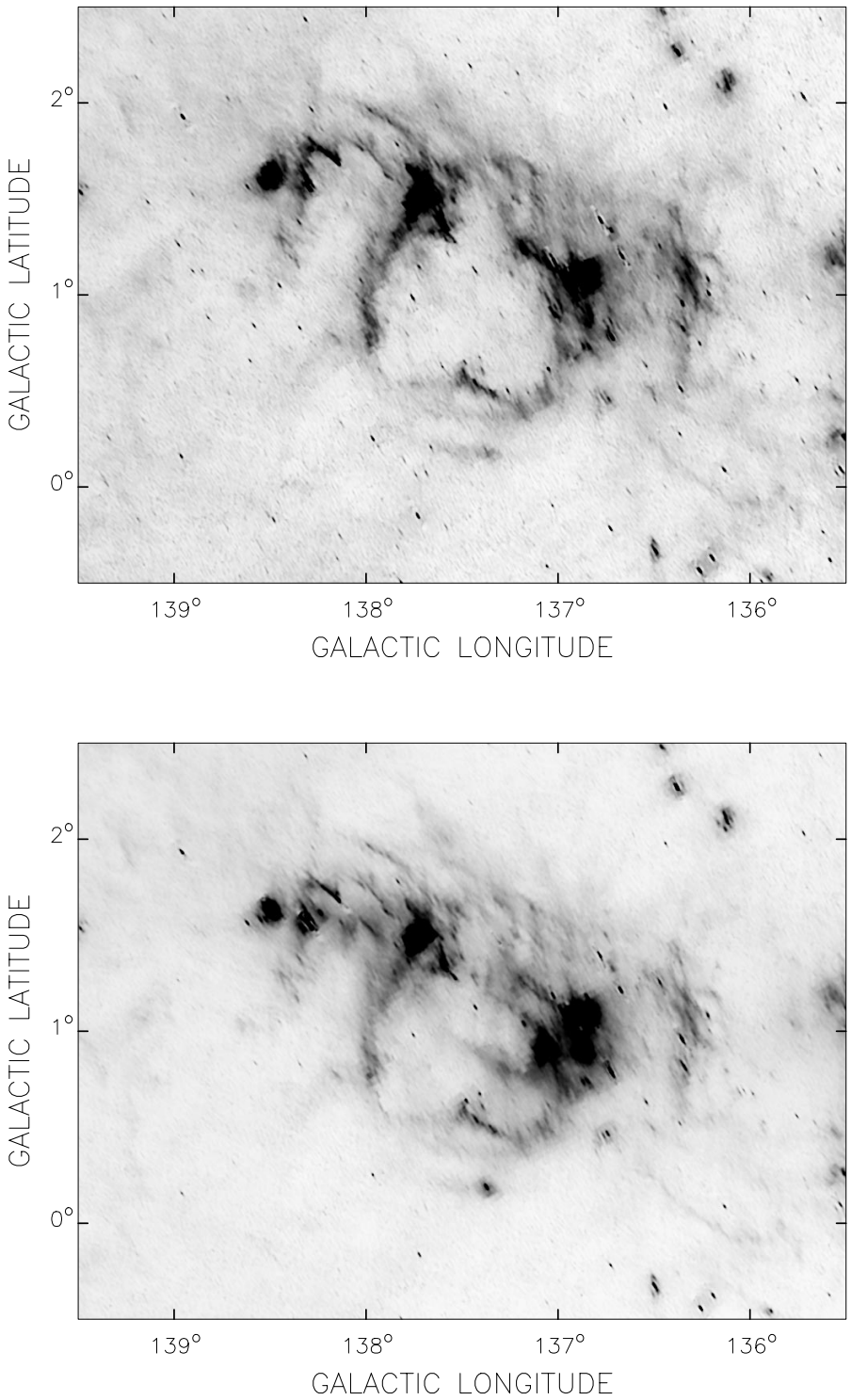

FIG. 11.—Two 4° × 3° mosaics of the W5 star forming region (*top*, 12 μm; *bottom*, 25 μm). The top image is linearly stretched from 2.7 to 16.1 MJy sr^{-1} (*white to black*) and the bottom image is linearly stretched from 6.0 to 29.2 MJy sr^{-1}.

the ease with which both the IGA and MIGA can be extended to higher or lower latitudes. Areas can also be mapped as separate regions using the same type of processing (e.g., the star-forming regions in Taurus and Ophiucus that are part of the IGA; IGA also includes Orion which was looked at by MSX).

Processing of regions outside of the CGPS survey area is currently underway, starting with the Rho-Oph star forming region and a H I structure at $l = 124°$. We intend to make users aware of the availability of these data via the CITA web pages.[9]

As demonstrated in § 4.2, cross-band resolution matching is a useful technique for the construction of large-scale high-resolution color ratio maps. Unfortunately, the means to do this sort of analysis is not available to the typical user of the

[9] http://www.cita.utoronto.ca/.

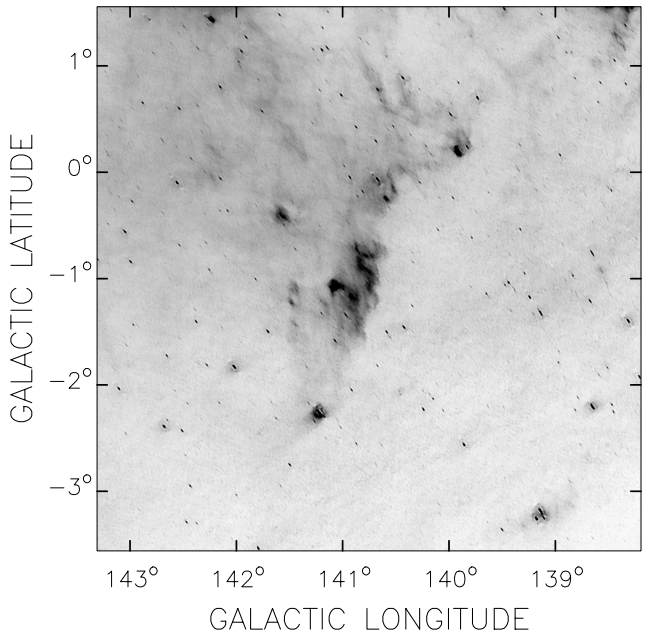

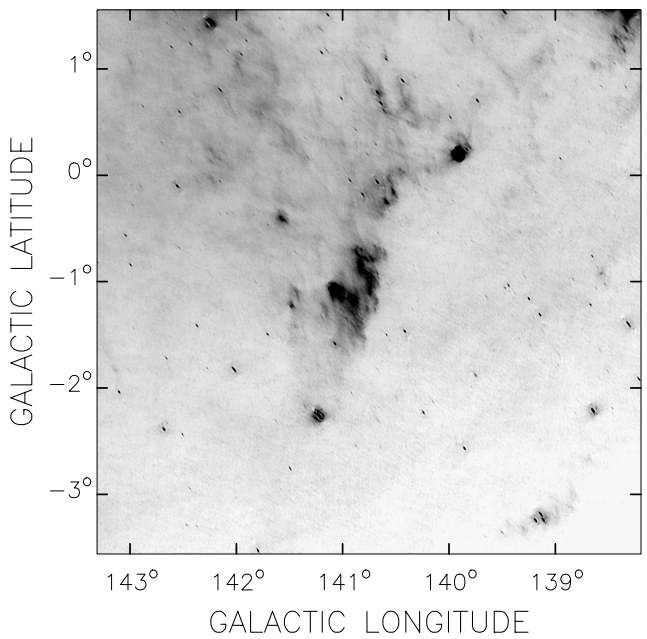

FIG. 12.—CGPS 5°.12 × 5°.12 mosaics demonstrating the utility of the MIGA in studying ISM structures of large angular extent (*top*, 12 μm; *bottom*, 25 μm). The feature in the center of the mosaic is infrared emission associated with the H II region LBN 140.8−1.4 (BFS 27 in Blitz et al. 1982). The top image is linearly stretched from 1.8 to 15 MJy sr^{-1}, and the bottom image is stretched from 5.3 to 17 MJy sr^{-1} (*white to black*).

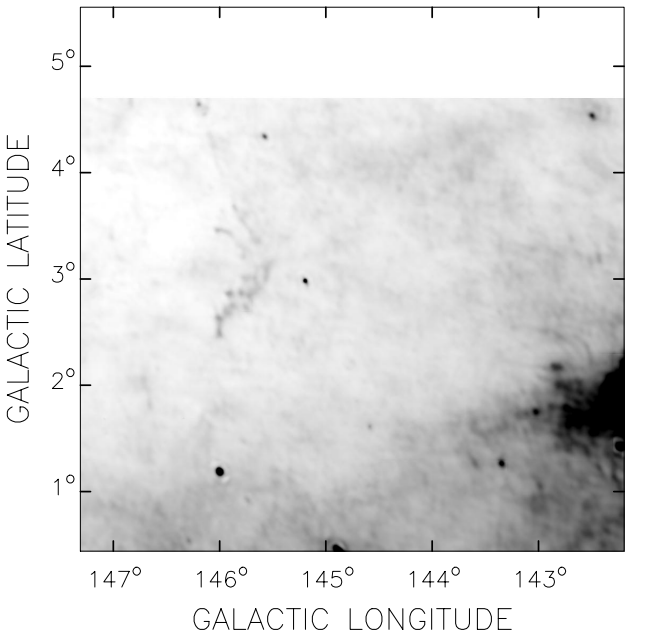

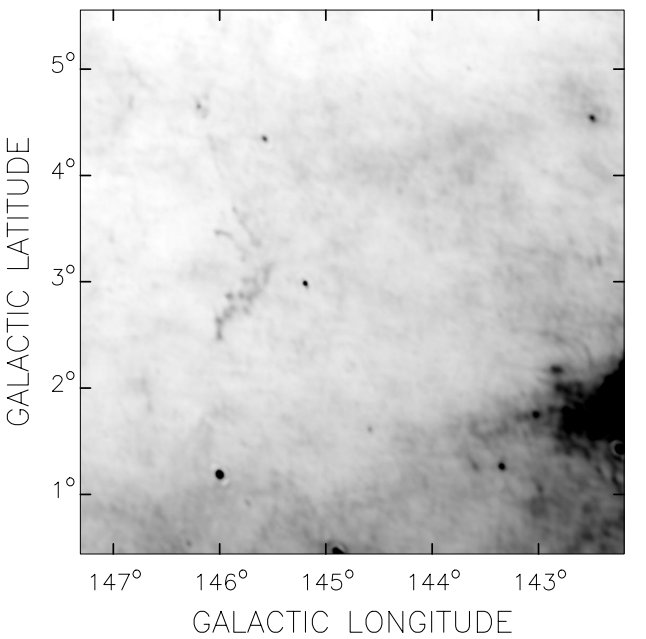

FIG. 13.—Extended IGA (EIGA). The top image shows a 100 μm CGPS mosaic region with the original extent of the IGA data. In order to provide full far-infrared coverage for the CGPS we constructed an extension to the IGA. The bottom image shows the same mosaic with the EIGA added on. Agreement between the IGA and EIGA was excellent. The applied linear stretch is from 24 to 120 MJy sr^{-1} (*top*) and 22 to 112 MJy sr^{-1} (*bottom*) (*white to black*).

MIGA. At the moment the only option is to request this sort of processing through IPAC or CITA (facilities with the *IRAS* data archive and the requisite software). We are currently working on techniques that will allow users to do cross-band simulations using the data that come as part of the MIGA and IGA. Once available this technique will greatly improve the utility of both HIRES data sets.

In summary, the MIGA provides users of the CGPS database with a mid-infrared data set that, combined with the IGA, will allow users to study infrared emission from the entire range of dust grain sizes and thus better study the evolution of dust grains as they move through different phases of the ISM. Both the MIGA and the IGA can be easily expanded and built upon to higher and lower Galactic latitudes and should continue to be useful in the study of disk-halo structures and star forming regions away from the Galactic plane where higher resolution infrared data over large angular scales are still not available.

We thank Yu Cao for his assistance and suggestions regarding the processing of the MIGA. Thanks also to Chas Beichman, Ron Beck, and Diane Engler at IPAC for their assistance in obtaining the raw *IRAS* archive, and John Fowler for discussions about the HIRES algorithms. C. R. K. would like to thank the Ontario Graduate Scholarship Program for support. This research was supported by the Natural Sciences and Engineering Research Council of Canada.

REFERENCES

Aumann, H. H., Fowler J. W., & Melnyk, M. 1990, AJ, 99, 1674
Basu, S., Johnstone, D., & Martin, P. G. 1999, ApJ, 516, 843
Blitz, L., Fich, M., & Stark, A. A. 1982, ApJS, 49, 183
Cao, Y., Eggermont, P. B., & Terebey, S. 1999, IEEE Trans. Image Processing, 8, 286
Cao, Y., Prince, T. A., Terebey, S., & Beichman, C. 1996, PASP, 108, 535
Cao, Y., Terebey, S., Prince, T. A., & Beichman, C. 1997, ApJS, 111, 387
English, J., et al. 1998a, Publ. Astron. Soc. Australia, 15, 56
English, J., et al. 1998b, BAAS, 30, 83.06
Fich, M., & Terebey, S. 1996, ApJ, 472, 624
Fowler, J. W., & Aumann, H. H. 1994, in Science with High Spatial Resolution Far-Infrared Data, ed. S. Terebey & J. Mazzarella (JPL 94-5; Pasadena: JPL), 1
Heiles, C. 1984, ApJS, 55, 585
IRAS Catalogs and Atlases: Explanatory Supplement. 1988, ed. C. A. Beichman, G. Neugebauer, H. J. Habing, P. E. Clegg, & T. J. Chester (Washington: GPO)
Moshir, M., et al. 1992, Explanatory Supplement to the *IRAS* Faint Source Survey, Version 2 (JPL D-10015; Pasadena: JPL)
Noriega-Crespo, A., Van Buren, D., Cao, Y., & Dgani, R. 1997, AJ, 114, 837
Normandeau, M., Taylor, A. R., & Dewdney, P. E. 1996, Nature, 380, 387
Onaka, T., Yamamura, I., Tanabe, T., Roellig, T. L., Yuen, L. 1996, PASJ, 48, 59L
Price, S. D. 1995, Space Sci. Rev., 74, 81
Rice, W. 1993, AJ, 105, 67
Wheelock, S. L., et al. 1994, *IRAS* Sky Survey Atlas Explanatory Supplement (JPL 94-11; Pasadena: JPL)